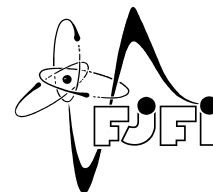




CZECH TECHNICAL UNIVERSITY IN PRAGUE
Faculty of Nuclear Sciences and Physical Engineering
Department of Physics



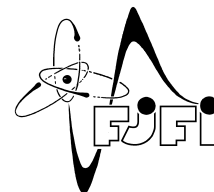
Bachelor thesis

Study of Diffraction Processes at LHC

Author: **Dagmar Bendová**
Supervisor: **Mgr. Marek Taševský, PhD.**
Academic year: 2015/2016



ČESKÉ VYSOKÉ UČENÍ TECHNICKÉ V PRAZE
Fakulta jaderná a fyzikálně inženýrská
Katedra fyziky



Bakalářská práce

Studium difrakčních procesů na LHC

Autor: **Dagmar Bendová**

Vedoucí práce: **Mgr. Marek Taševský, PhD.**

Akademický rok: 2015/2016

Prohlášení:

Prohlašuji, že jsem svou bakalářskou práci vypracovala samostatně a použila jsem pouze podklady (literaturu, projekty, software, atd.) uvedené v příloženém seznamu.

Nemám závažný důvod proti použití tohoto školního díla ve smyslu §60 Zákona č. 121/2000 Sb., o právu autorském, o právech souvisejících s právem autorským a o změně některých zákonů (autorský zákon).

V Praze dne 7.7.2016

Dagmar Bendová

Title:

Study of Diffraction Processes at LHC

Author: Dagmar Bendová

Specialization: Experimental Nuclear and Particle Physics

Sort of the project: Bachelor thesis

Supervisor: Mgr. Marek Taševský, PhD., Institute of Physics of the Academy of Sciences of the Czech republic

Abstract: Diffraction processes represent a large contribution to the total inelastic cross-section in proton-proton collision. It is therefore very important to understand these processes to provide a better description of the experimental data from LHC experiments. This thesis is devoted to study of diffraction. Particularly properties of the diffraction were studied in inclusive events and in cases with at least two jets with $p_T > 20$ GeV simulated by MC generator Pythia 8.186 at the center-of-mass energy $\sqrt{s} = 7$ TeV. The distribution of fractional momentum loss of the incident proton for various pomeron fluxes is studied. Then other observables are discussed for Minimum Bias Rockefeller flux, namely square of the four-momentum transfer, invariant mass of the diffractive system and number of charged particles. Finally, the distribution of the rapidity gap size as published by ATLAS for both inclusive and dijet events is compared with predictions of Pythia 8 using single diffractive, double diffractive and non-diffractive processes and observed differences are briefly discussed.

Key words: diffraction, jets, MC generator Pythia 8, pomeron, rapidity gaps

Název práce:

Studium difrakčních procesů na LHC

Autor: Dagmar Bendová

Obor: Experimentální jaderná a částicová fyzika

Druh práce: Bakalářská práce

Vedoucí práce: Mgr. Marek Taševský, PhD., Fyzikální ústav AV ČR, v.v.i.

Abstrakt: Difrakční procesy představují vysoký příspěvek k celkovému neelastickému účinnému průřezu v proton-protonových srážkách. Proto je velmi důležité těmto procesům porozumět a poskytnout tak lepší možnosti popisu dat z experimentů na urychlovači LHC. Tato práce se věnuje studiu právě difrakčních procesů. Konkrétně jsou vlastnosti difrakce zkoumány v inkluzivních případech a případech s podmínkou na existenci alespoň dvou jetů s příčnou hybností $p_T > 20$ GeV, které byly simulovány pomocí MC generátoru Pythia 8.186 při těžišťové energii $\sqrt{s} = 7$ TeV. Rozdělení frakce hybnosti protonu ztracené při srážce je diskutováno pro několik různých možností volby fluxu pomeronu. Pro flux Minimum Bias Rockefeller jsou diskutovány další veličiny, jmenovitě kvadrát přenesené hybnosti, invariantní hmota difrakčního systému a počet nabitých částic. Dále jsou rozebrány a porovnány s daty kolaborace ATLAS předpovědi pro jednoduchou a dvojitou difrakci, nedifrakční události a celkový neelastický diferenciální účinný průřez v závislosti na velikosti prázdné oblasti v detektoru.

Klíčová slova: difrakce, jety, MC generátor Pythia 8, pomeron, prázdné oblasti v detektoru

Acknowledgment:

I would especially like to express my great gratitude to my supervisor Dr. Marek Taševský for his guidance, provided knowledge, many useful remarks and corrections and enormous patience during my work on this thesis. I would also like to thank my family and friends for their support and psychic comfort they are giving to me.

Contents

Introduction	9
1 Standard Model of Particle Physics	11
1.1 Interactions and Elementary Particles	11
1.2 Quantum Chromodynamics	12
2 Diffraction	15
2.1 Regge theory	16
2.2 Soft Diffraction	17
2.3 Hard Diffraction	18
3 The Large Hadron Collider and the ATLAS Detector	23
4 Monte Carlo Generators and Jets	27
4.1 MC Generators	27
4.1.1 Pythia 8	28
4.2 Jets	28
5 Results	31
5.1 Transverse energy flow in the ATLAS detector	31
5.2 Pomeron flux in inclusive and dijet single diffractive events	34
5.3 Characteristic particle properties of diffractive events	37
5.3.1 Inclusive events	38
5.3.2 Dijet events	40
5.4 Rapidity gaps - inclusive and dijet and comparison with the data	42
Conclusion	47
Bibliography	48

Introduction

As the diffraction creates a considerable contribution to the inelastic cross-section in high-energy collisions of hadrons, it is very important to develop and improve its theoretical description in order to better understand the experimental results. The H1 Collaboration at HERA accelerator brought new results on the diffraction occurring in deep inelastic scattering in ep collisions. Very precise measurements were executed which led to the improvement of the understanding the diffractive processes. This success was followed by experiments at the Tevatron, where protons and antiprotons were collided, and even more precise results and new observations were acquired. With the construction of the Large Hadron Collider at CERN new and even more precise results have been expected and diffraction in pp collisions is now an object of interest of the large part of particle physics community as it can provide further improvements in our understanding of the Standard Model and physics beyond it.

A brief introduction to Standard Model of particle physics and quantum chromodynamics is provided in Chapter 1. Chapter 2 summarizes the classes and main properties of diffractive processes, an outline of the Regge theory and soft diffraction phenomenology is then provided and also a short overview of the hard diffraction description is presented to the reader. Large Hadron Collider and the ATLAS experiment is briefly described in Chapter 3. Chapter 4 provides an introduction to Monte Carlo event generators and mentions Pythia 8 generator which is later used for the simulation of diffractive events. As this thesis deals also with diffractive events in which hard-scale objects called jets appear, a summary on jets, their properties and algorithms used for their reconstruction is also provided in Chapter 4.

Finally in Chapter 5 author's own experimental work is presented. First of all a transverse energy flow through the ATLAS detector is examined and sum of the transverse energies $\sum E_T$ and transverse energy density $E_T^{density}$ are compared to the ATLAS data in six regions of pseudorapidity. The rest of the Chapter 5 is devoted solely to the diffractive properties. Various pomeron fluxes available in Pythia 8 settings are compared for the distribution of fractional momentum loss of the incident proton ξ and after that diffractive properties such as square of the four-momentum transfer t , invariant mass M_X or number of charged particles n_{ch} are compared in inclusive and dijet events for the Minimum Bias Rockefeller flux choice. In the end we focus on the contribution of single diffraction, double diffraction and non-diffractive processes to the differential inelastic cross-section depending on the rapidity gap size in inclusive and dijet events and its comparison with the ATLAS data.

Chapter 1

Standard Model of Particle Physics

There has always been a tendency of unifying the known independently looking physics laws and observations into a more general theoretical description. The Standard Model is the most successful description of the microworld nowadays, confirmed by many experiments. It is a quantum field theory based on a $SU(3) \times SU(2) \times U(1)$ non-abelian gauge symmetry unifying the electroweak theory and quantum chromodynamics (QCD). However it can not be accepted as the final unifying theory because it does not comprehend the gravitational interaction and can not explain the origin of the necessary input parameters, e.g. the properties of the elementary particles.

1.1 Interactions and Elementary Particles

Standard Model describes the electromagnetic, weak and strong interaction between fermions through the exchange of 12 mediating bosons with an integer spin equal to 1. Fermions have a half integer spin $\frac{1}{2}$ and can be further divided into leptons and quarks which form three families. Also for each fermion there exists a corresponding anti-particle. Leptons consist of three charged particles - electron (e^-), muon (μ^-) and tauon (τ^-) - and three electrically neutral particles - electron neutrino (ν_e), muon neutrino (ν_μ) and tauon neutrino (ν_τ). Each lepton family is represented by one charged lepton and corresponding neutrino. Neutrinos are considered to be massless according to SM, however the observations of neutrino oscillation suggest that they should have a non-zero mass [1]. Besides the electric charge, which allows charged leptons to interact through the electromagnetic force, each lepton also carries a weak charge allowing them to interact via the weak force, which is the only force through which neutrinos can interact with the matter. Each quark family consists of one quark with the electric charge $-\frac{2}{3}$, which are up (u), charm (c) and top (t), and one with the electric charge of $-\frac{1}{3}$, which are down (d), strange (s) and bottom (b). Like leptons, they also possess a weak charge. Moreover quarks have a non-zero quantum number colour (often called "colour charge") which allows them to interact via strong force and thus create composite particles called hadrons, further divided into baryons compound of three quarks and mesons compound of one quark and one anti-quark. There are three colours - red, green, blue - and corresponding anti-colours.

The strong force is mediated by 8 gluons (g) which are electrically neutral and massless. They also carry one of the eight allowed combinations of colour and anti-colour which enables them not only to change the colour of quarks, but also to interact with themselves. This is a very important feature which has further consequences and will be discussed later in the section dedicated to the QCD. The strong force increases with growing distance and therefore it is not possible to observe free quarks under normal conditions. However at small distances, they appear as almost free particles. This state is called

an asymptotic freedom and gives rise to a quark-gluon plasma state. The electromagnetic interaction is mediated by a photon (γ) which is also massless and thus the EM force has an infinite range. Two electrically charged bosons W^\pm and one neutral boson Z^0 which interact with the field through the weak hypercharge Y are responsible for existence of the weak force. Because of the relatively great mass of its intermediating bosons, the weak force has a short range. The fermions and bosons gain their masses through a spontaneous symmetry breaking mechanism. This mechanism is accompanied by the appearance of a heavy scalar particle called the Higgs boson which was predicted in the 1960s and its existence has successfully been confirmed in 2012 at the LHC [2], [3] completing the experimental confirmation of the SM predictions. A summary of the elementary particles and gauge bosons along with their properties can be seen in Figure 1.1.

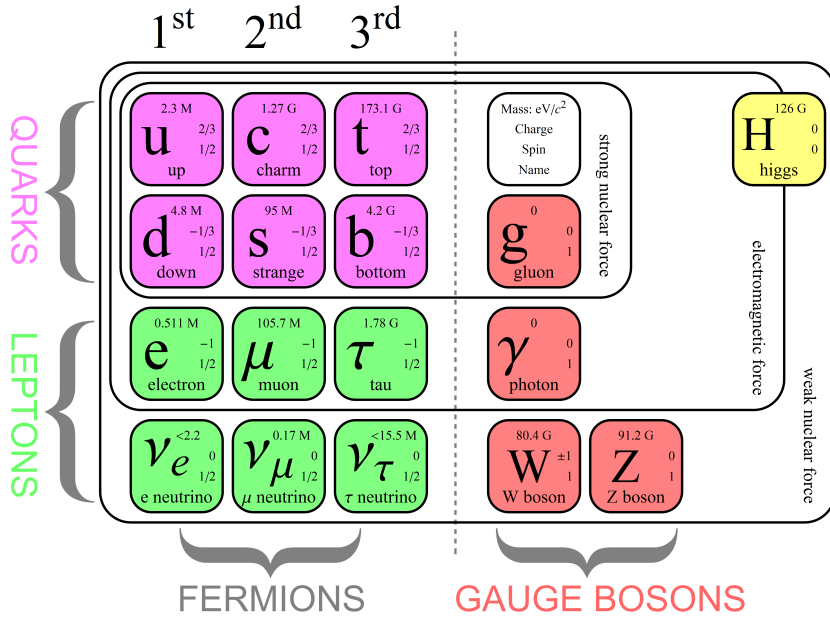


Figure 1.1: An overview of elementary particles and gauge bosons of the SM with their basic properties. Taken over from [4].

1.2 Quantum Chromodynamics

The strong nuclear force, mentioned above, is described by the means of quantum chromodynamics (QCD). It is a quantum field theory described by the Lagrangian which is invariant under a local gauge transformation $SU(3)$ and gives rise to eight massless vector bosons - gluons - which act as mediators of the strong interaction. The QCD Lagrangian can be written as

$$\mathcal{L}_{QCD} = -\frac{1}{4}F_{\mu\nu}^a F^{a\mu\nu} + \sum_k^{n_f} \bar{\psi}_k^j (i\not{D} - m)_{ij} \psi_k^j + \mathcal{L}_{gauge} + \mathcal{L}_{ghost} \quad (1.1)$$

with

$$F_{\mu\nu}^a = \partial_\mu A_\nu^a - \partial_\nu A_\mu^a + g f^{abc} A_\mu^b A_\nu^c \quad (1.2)$$

$$(D_\mu)_{ij} = \delta_{ij} \partial_\mu - \frac{i}{2} g A_\mu^a \lambda_{ij}^a \quad (1.3)$$

where indices $a \in 1, \dots, 8$ mark the massless gluon fields A_μ^a which mediate the strong interaction among the quark fields ψ_k^i (or ψ_k^j), i, j runs over 3 colours and k denotes the flavour of the quark. The term (1.2) is called a kinetic term and is responsible for the gluon self-interaction. Through the Gell-Mann matrices λ_{ij}^a , the SU(3) colour group generators are related to structure coefficients f^{abc} . The term (1.3) ensures the local gauge invariance of the \mathcal{L}_{QCD} . In order to define the gluon propagator and allow the perturbative calculations, a proper gauge must be chosen and introduced to the QCD Lagrangian in Eq. (1.1) as a \mathcal{L}_{gauge} . Ghost scalar fields \mathcal{L}_{ghost} must be then added to Eq. (1.1) to cancel out the unphysical degrees of freedom of the gluon fields. The detailed explanation of the QCD Lagrangian and the field theory behind it can be found in [5].

In order to obtain the scatter amplitudes of the process, a perturbative theory can be used with the strong coupling parameter $\alpha_s(Q^2)$ used as the expansion parameter. Therefore it must be much lower than unity if perturbative series are to be used to predict physical quantities at any order. The calculation at the leading order (LO) gives satisfactory results, however at higher orders ultraviolet and infrared divergences can appear. These divergences are caused by the integration over the momenta of particles which create a loop in the Feynman diagram representing certain process. To remove these divergences from the calculation a renormalization process must be performed. Using this renormalization process, one can predict the dependency of the coupling constant α_s of the strong interaction on the transfer four-momentum square Q^2 in the leading order as follows

$$\alpha_s(Q^2) = \frac{4\pi}{11 - \frac{2}{3}n_f \ln\left(\frac{Q^2}{\lambda_{QCD}}\right)} = \frac{1}{B \ln\left(\frac{Q^2}{\lambda_{QCD}}\right)} \quad (1.4)$$

where $\lambda_{QCD} \approx 200$ MeV is a scale parameter at which the perturbative calculations are not usable anymore. The B parameter, with n_f being the number of quark flavours, causes α_s to decrease with the growing momentum transfer. Therefore α_s is often called a "running constant" as it is changing its value with the change of Q^2 scale. It causes the confinement of the quarks and gluons within hadrons at large distances (low Q^2) and at small distances (high Q^2) the state called asymptotic freedom is observed and the perturbative calculations can be used at this scale.

The proton inner structure and behavior can be described by the structure functions investigated during various scattering experiments. Particles forming the inner structure were called partons and they have later been associated with quarks and gluons. Partons in nucleon are described by the parton distribution function $f_i(x, Q^2)$ which gives us the probability that parton i with virtuality Q^2 carries longitudinal momentum fraction x of the proton, where x is the Björken variable which is used to characterize parton's kinematic properties as a fraction of the proton's ones. The important feature used in calculation of cross-sections is that a process cross-section can be expressed as a convolution of PDFs of participated partons and corresponding sub-process cross-section, i.e. it can be factorized.

Deep Inelastic Scattering (DIS) experiments played a key role in investigating the parton model and were one of the first tests of QCD description. Especially DIS experiments performed on the HERA ep collider played a key role in probing the diffractive structure functions and parton distribution functions. More information on scattering experiments, parton model, structure functions and their evolution equations, QCD and SM can be found in sources [5], [6], [7] and [8].

Chapter 2

Diffraction

The total hadron-hadron (pp) interaction cross-section can be divided into two parts. First one corresponds to elastic processes in which both protons are only rescattered and therefore remain intact. Inelastic processes are responsible for the second part of the cross-section. One or both protons are dissociated and the production of new particles occurs during inelastic processes. Diffractive processes form a significant contribution to the total inelastic cross-section and therefore it is very important to understand the mechanism behind them.

Diffraction is considered to be a quasi-elastic process and can be explained as an exchange of the object with quantum numbers of vacuum, thus being a colorless object, called pomeron (named after Isaak Y. Pomeranchuk). There are several various approaches describing the pomeron and they will be briefly introduced in following sections. A distinctive feature of diffractive processes is the presence of large rapidity gap (LRG) which is a region in pseudorapidity devoid of any hadronic activity. Despite the "rapidity" in the name, a pseudorapidity η variable is being used in the calculation of a gap size $\Delta\eta$. Pseudorapidity η is in high-energy limit approximately equal to rapidity y and is defined as

$$\eta = -\ln \tan\left(\frac{\theta}{2}\right), \quad (2.1)$$

where θ is a polar angle measured from the z axis (i.e. beam direction).

We distinguish several classes of diffractive processes which are depicted in Figure 2.1. Single diffraction (SD) is the most frequent of them and also the easiest one to detect. In this process, one of the protons remain intact and is only rescattered in forward direction (i.e. with large η) and the other proton dissociates into a hadronic system X carrying the quantum numbers of the original proton. The system X is separated from the forward proton by the large rapidity gap. If both interacting protons are broken, we talk about the double diffraction (DD). Two final state hadronic system X and Y , both carrying quantum numbers of the original protons, are created and a rapidity gap separates them. The third class of diffractive events is the central diffraction (CD) composed of double pomeron exchange (DPE) and central exclusive production (CEP) where both protons remain intact and a system X with quantum numbers of vacuum is created in the central region, separated by a rapidity gap from each of the rescattered protons. Unlike in DPE, in CEP both pomerons go into the hard sub-process with all their four-momenta and leave no pomeron remnants. Also a multiple pomeron exchange may occur but the process is very rare and difficult to detect.

Diffraction is dominated by soft processes with small momentum transfer which are described by phenomenological models based on the Regge theory, because a perturbative approach of QCD can not be used at this level. At hard scale a pQCD can be used and the pomeron is introduced in terms of QCD

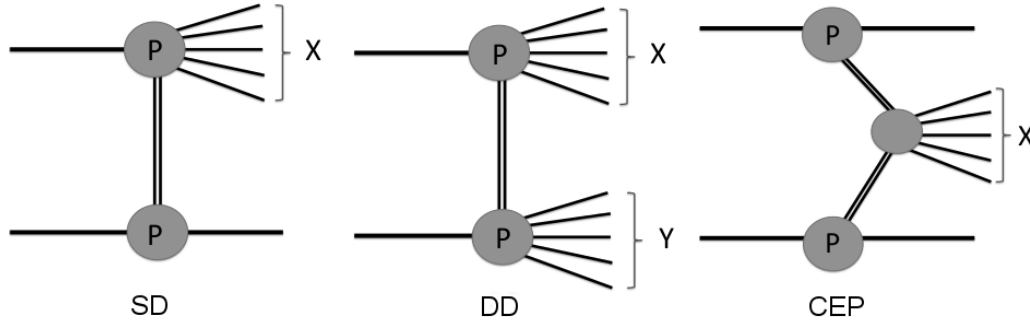


Figure 2.1: The three most important types of diffractive processes, single diffraction on the left, double diffraction in the middle and central diffraction on the right. [9]

as a color singlet object with vacuum quantum numbers created by an exchange of two interacting gluons. It is therefore obvious that the soft and hard pomeron have different properties. Pomeron is considered to have an internal structure and can be described by diffractive parton density functions (DPDF) similar to common particle PDFs. Various high transverse momentum objects can be produced in diffractive processes, the most interesting is a jet production. The diffraction is very important for studying the low- x structure of the proton or it can provide an environment for the Higgs boson production. Also it is very useful in the physics of heavy-ion collisions where it provides a useful tool for investigating the QCD dynamics in high-density regime and the related saturation effect.

2.1 Regge theory

Regge theory was developed in late 1960s as a theory describing the strong interactions. Although it was succeeded by quantum chromodynamics, it still holds its importance for the elastic scattering and description of the diffraction. Regge theory is based on analytical properties of scattering amplitudes $A(i \rightarrow f)$ and thus on properties of the S-matrix. S-matrix is a unitary linear operator which allows us to evolve the initial state $|i\rangle$ into the final state $|f\rangle$, hence

$$S|i\rangle = |f\rangle. \quad (2.2)$$

Using the scattering amplitude and unitarity of S-matrix one can obtain a so called optical theorem which is one of the key relations for Regge theory construction. It relates the total cross section and elastic scattering amplitude $A(s, t)$ of the process $1 + 2 \rightarrow 1 + 2$ by equation

$$\sigma_{12}^{tot} = \frac{1}{2|\mathbf{p}_1| \sqrt{s}} \text{Im}A(s, t = 0) \quad (2.3)$$

where $|\mathbf{p}_1|$ is a size of the initial center-of-mass frame momentum and s and t are the Mandelstam variables.

For the construction of Regge theory, we expand the scattering amplitude in the s -channel using the partial-waves series as

$$A(s, t(s, z_s)) = 16\pi \sum_{l=0}^{\infty} (2l+1) A_l(s) P_l(z_s) \quad (2.4)$$

$$A_l(s) = \frac{1}{32\pi} \int_{-1}^{+1} P_l(z_s) A(s, t(s, z_s)) dz_s \quad (2.5)$$

where $z_s = \cos(\theta_s)$ with θ_s being the scattering angle and $P_l(z_s)$ are the Legendre polynomials of order l . The partial-wave series can be analogously written in t -channel, however as $s \rightarrow \infty$ the series diverges. Regge solved this problem introducing the angular momentum l as a continuous complex variable. Therefore the partial wave amplitude $A_l(t)$ can be seen as a function of complex l . Under certain assumptions (see [10]), the singularities of $A_l(t)$ in the complex plane are poles (called Regge poles) with locations varying as

$$l = \alpha(t) \quad (2.6)$$

which is usually approximated by the Taylor series around $t = 0$ using its first two terms as

$$\alpha(t) = \alpha(0) + \alpha' t. \quad (2.7)$$

The Regge poles, which are interpreted as resonances of increasing angular momentum l , and functions $\alpha(t)$, which interpolate those resonances, are called Regge trajectories or reggeons. Interaction is then described as an exchange of reggeons. The first term in (2.7) is called reggeon intercept and α' is a reggeon slope of the trajectory. Scattering amplitudes are then correspondingly rewritten with respect to the Regge poles and one can obtain a prediction for the total cross-section of simple reggeon exchange using the optical theorem (2.3) as

$$\sigma^{tot} \approx s^{\alpha(0)-1}. \quad (2.8)$$

Based on this relation, the total cross-section should decrease with an increasing energy. However this behavior was not confirmed by the experiments and in order to obtain the behavior of the total cross-section actually observed in experiment, a trajectory dominant in high energies with intercept $\alpha(0) < 1$ was introduced. This new trajectory with quantum numbers of vacuum was named pomeron and does not correspond to any known particle. A small deviation from unity, labeled as ϵ was shown by the data. Donnachie and Landshoff later introduced the description of the total cross-section dependency on center-of-mass energy \sqrt{s} using a Regge-based parametrization

$$\sigma^{tot} = X s^{0.0808} + Y s^{-0.4525} \quad (2.9)$$

where X and Y are free parameters, first term corresponds to pomeron exchange and second can be interpreted as a reggeon contribution. More detailed information on Regge theory and its development can be seen in [9], mainly in [10] and also in [11].

2.2 Soft Diffraction

For the soft diffractive processes a pQCD approach can not be applied due to small momentum transfer. However we can use a Regge theory based phenomenological models. To show the basic approach, let us consider a single diffractive process

$$a + b \rightarrow c + X$$

in which the pomeron exchange is the dominant mechanism. The process can be interpreted as an interaction of a pomeron, radiated from particle a , with the particle b which dissociates into a hadronic system X . Particle a loses a very small fraction ξ (also labeled as $x_{\mathbb{P}}$) of its momentum and is rescattered

as a particle c which thus has its longitudinal momentum fraction $x_L = 1 - \xi$ close to its maximum value 1. A large rapidity gap with size $\Delta\eta$, which satisfies

$$\Delta\eta \approx -\ln\xi, \quad (2.10)$$

emerges between the particle c and the hadronic system X whose invariant mass is M_X . Also the Mandelstam variable

$$t = (p_a - p_c)^2 \quad (2.11)$$

which is the squared four-momentum transfer is crucial for the description.

From the process amplitude (in the sense of Regge theory) one can calculate a (factorized) cross-section of the process. We will acquire

$$\frac{d^2\sigma}{d\xi dt} = f_{\mathbb{P}/a}(\xi, t) \cdot \sigma^{\mathbb{P}b}(M_X^2, t) \quad (2.12)$$

where the first part is the pomeron flux factor denoting to the probability of a pomeron being radiated from particle a , and second term is the cross-section for the pomeron scattering on particle b , both defined as

$$f_{\mathbb{P}a}(\xi, t) \equiv f_{\mathbb{P}}(\xi, t) = \frac{9\beta_{\mathbb{P}}^2}{4\pi^2} (F_1(t))^2 \xi^{1-2\alpha_{\mathbb{P}}(t)} \quad (2.13)$$

$$\sigma^{\mathbb{P}b}(M_X^2, t) = X^{\mathbb{P}b}(t) \cdot (M_X^2)^\epsilon + Y_+^{\mathbb{P}b}(t) \cdot (M_X^2)^{\eta_+}. \quad (2.14)$$

The first term in (2.14) represents the pomeron exchange which contributes to the cross-section (2.12) as a triple-pomeron vertex in which three pomerons are coupled together. The second term contributes with the non-leading exchanges which can be neglected for very large M_X^2 . The outcome of the Eq. (2.12) might suggest that pomeron is a particle, however it is not so. Pomeron is not a real particle and it also do not correspond to any known particle. It is considered to be "like" a particle in the terms of Regge theory and subsequent phenomenological models. Analogically the cross-section for double diffraction can be obtained. The double pomeron exchange process is also very interesting since its limiting case, the central exclusive production, may lead to the production of Higgs boson. The detailed description of the soft diffractive phenomenology is provided in [10].

2.3 Hard Diffraction

Passing on to the hard scale of the process and thus to higher energies allows us to investigate the partonic structure of interacting particles, especially if the interaction contains jets in the final state. The probability of the proton emitting the pomeron in hard diffraction is also based on Regge theory, however the trajectory $\alpha(t)$ is different and the pomeron is considered to be a compound object with inner partonic structure. Using the hard scale of the interaction, perturbative approach can be used and it is also possible to measure and determine diffractive parton distribution functions (DPDF) of the proton $f^D(x, Q^2, \xi, t)$ which can be considered as a conditional probability to find a parton i with fractional momentum $x\xi$ inside the proton during the diffractive process. The cross-section of a hard diffractive process can be expressed as a convolution of DPDF and a cross-section $\sigma_i(x, Q^2)$ of the hard partonic sub-process

$$d\sigma = \sum_i f_i^D(x, Q^2, \xi, t) * d\sigma_i(x, Q^2). \quad (2.15)$$

The DPDF can be further decomposed into pomeron flux $f_{\mathbb{P}}(\xi, t)$ and pomeron distribution function $f_i^{\mathbb{P}}(x, Q^2)$, which gives a probability to find a parton i inside the pomeron, as

$$f_i^D(x, \xi, t, Q^2) = f_{\mathbb{P}}(\xi, t) \cdot f_i^{\mathbb{P}}(x, Q^2). \quad (2.16)$$

Fractional momentum loss ξ of the incident proton can be expressed as

$$\xi = \frac{(P - P') \cdot q}{P \cdot q} \quad (2.17)$$

where P and P' are the initial and final four-momenta of the proton and q is the transferred four-momentum. The square of the four-momentum transfer t is the Mandelstam variable defined as

$$t = (E - E')^2 - (\mathbf{p} - \mathbf{p}')^2 \quad (2.18)$$

where E and E' are the initial and final energies of the proton and \mathbf{p} and \mathbf{p}' are the initial and final momenta.

Momentum fraction $z_{\mathbb{P}}$ of the pomeron carried by the parton which enters the hard process and interacts with the parton from the proton is expressed using the scale of the process Q^2 and invariant mass M_X of the final state system as

$$z_{\mathbb{P}} = \frac{Q^2}{Q^2 + M_X^2} \quad (2.19)$$

and can be related to the ξ and the Björken variable x using the equation $x = z_{\mathbb{P}}\xi$. A schematic diagram of a typical hard single diffractive process with production of two jets in the diffractive final state system X is depicted in Figure 2.2.

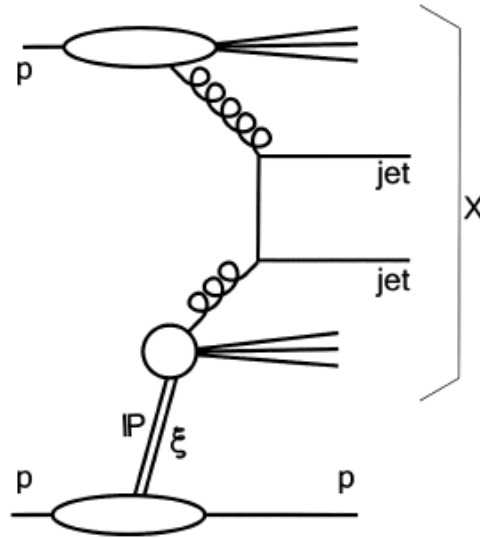


Figure 2.2: A schematic diagram of hard single diffractive scattering in hadron-hadron collisions. [12]

First case of hard diffractive process accompanied by high- p_T jets was experimentally observed by the UA8 collaboration in $p\bar{p}$ collisions at CERN [13]. This measurement opened the new possibilities for the description of the hard diffraction scattering in terms of diffractive parton distribution functions and led to its proper investigation.

Important progress in understanding the diffraction at the hard scale was carried out in the DIS experiments performed by H1 and ZEUS collaborations at HERA. A schematic diagram of the diffractive DIS can be seen in Figure 2.3.

NLO QCD fits [14] for gluon and quark densities

$$z f_i^{\mathbb{P}}(z, Q^2) = A_i z^{B_i} (1-z)^{C_i} \quad (2.20)$$

where z is the longitudinal momentum fraction of the proton carried by the parton which interacts in the sub-process, f_i is the DPDF and A_i , B_i and C_i are the fit parameters. These fits performed on diffractive DIS data are denoted as "H1 2006 DPDF Fit A" and "H1 2006 DPDF Fit B". In both of them majority of the pomeron momentum is carried by gluons at small z and quarks have very small contribution. These results led to the predictions for the diffractive processes behavior in $p\bar{p}$ collisions at Tevatron which are depicted in Figure 2.4 along with the Tevatron data. As we can see, the Tevatron data are suppressed by an approximately constant factor 10 when compared to the expectations based on the HERA data. Depicted results carried by the CDF Collaboration showed the so called factorization breaking in hadron-hadron collisions caused by additional soft partonic interactions. Equation (2.15) express the QCD factorization of the cross-section and although it works perfectly for ep collisions at HERA and therefore it was believed that DPDFs measured at HERA are universal, Figure 2.4 shows us a significant disagreement. As the factorization is broken in proton-antiproton collisions, diffractive parton distribution functions measured at HERA can not be considered universal, i.e. they do not provide proper predictions for other diffractive experiments.

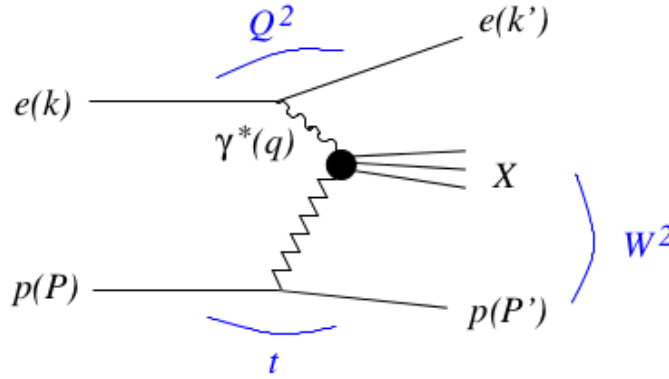


Figure 2.3: Schematic diagram of inclusive deep inelastic scattering. Particle's four-momenta are labeled in parentheses. [15]

The gap survival probability factor S^2 was introduced as a probability that the soft interactions do not spoil the gap and event survives them. The diffractive hadron-hadron cross-section is then defined as the cross-section of hard diffractive scattering multiplied by the S^2 factor. The soft survival probability was found to be $S^2 \approx 0.1$ in Tevatron single diffraction dijet events and using the so called KMR model it was predicted to be similar or slightly smaller in the LHC collisions at $\sqrt{s} = 7$ TeV.

Diffractive dijet measurements carried out by the CMS Collaboration and compared with predictions of MC event generators gave two compatible results, namely $S^2 \approx 0.12 \pm 0.04$ and $S^2 \approx 0.08 \pm 0.04$, when compared to the LO (resp. NLO) matrix elements, which seems to be in an agreement with the theoretical prediction [16].

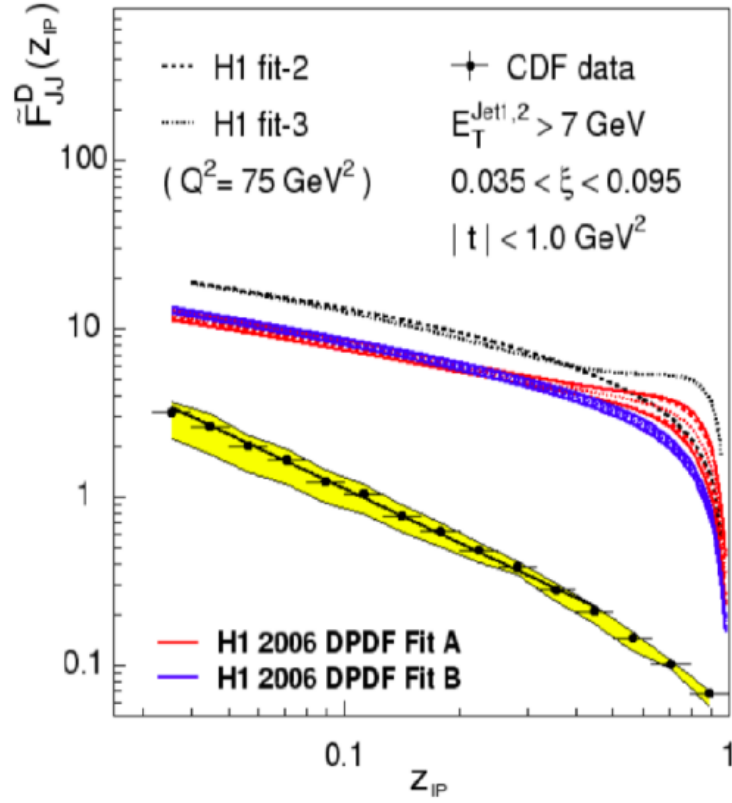


Figure 2.4: Tevatron data (yellow band) on the DPDFs as a function of the momentum fraction carried by the parton from the pomeron involved in hard sub-process compared to the predictions based on the H1 measurements. [18]

Also the ATLAS Collaboration estimation [12] $S^2 = 0.16 \pm 0.04$ (stat.) ± 0.08 (exp. syst.), which is based on the comparison of the data and predictions of the MC models based on DPDFs, shows a reasonable agreement with both theoretical prediction and CMS result.

The ATLAS Collaboration members also published several other measurements of the diffractive processes of which already mentioned paper [12], related thesis [16] and paper [17] will form the basis of the results presented in this thesis.

Chapter 3

The Large Hadron Collider and the ATLAS Detector

The LHC is probably the biggest scientific tool in the world ever built. This 27 kilometers long circular accelerator was constructed using the already existing infrastructure and tunnel of the LEP accelerator between 1998 and 2008 by the European Organization for Nuclear Research (also known as CERN) to test the predictions of the Standard Model and the theories beyond it. The accelerator is placed in the tunnel 175 meters beneath the ground near Geneva. It consists of two beam pipes filled with ultrahigh vacuum - approximately $10^{-10} - 10^{-11}$ mbar - in which the particles travel in opposite directions crossing in one of the four interaction points where the main detectors are placed. The beam pipes are surrounded by more than 1600 various superconducting electromagnets kept at the temperature -271.3 °C, which guide the beam along its path through the collider. A total of 1232 dipole magnets 15 meters in length are used to bend the beam, 392 quadrupole magnets serve to focus the beam and other more precise magnets are used to adjust the quality and precision of the beam to provide better chances of successful collisions.

The LHC is designed to be capable of colliding protons at various center-of-mass energies up to the highest planned one $\sqrt{s} = 14$ TeV. It can also collide protons with the lead nuclei and the lead nuclei themselves. The whole accelerating process is realized by several other machines which preaccelerate the particles before its injection to the LHC. The schema of this accelerators system can be seen in Figure 3.1. First of all, the hydrogen atoms are taken from the storing bottles and their orbital electrons are stripped off. The resulting protons are accelerated to 50 MeV in Linac2 and then injected into the Booster which accelerates them to 1.4 GeV. After that the Proton Synchrotron takes its turn in acceleration of the beam to 25 GeV then protons are sent to the Super Proton Synchrotron where they are accelerated to 450 GeV and in the end they are finally injected into the LHC beam pipes where they are accelerated to its final energy before the collision. This whole process serves not only to gradual acceleration of the particles but also to prepare the bunches of the protons for the collision. Bunches are used because its very complicated and technically demanding to direct two sole protons against each other. The LHC machine is designed to be filled by approximately 2800 bunches located in the beam pipe, which are being collided every ≈ 25 ns, each of them containing of the order of 10^{11} protons. Such a procedure may lead to multiple interactions per collision resulting in a detection of the particles which came from not only one event and thus so called pile-up arises. It is therefore very important to study these pile-up cases to be able to perform a proper corrections so we can examine only those events which we are interested in.

During its operation the LHC produces a large amount of data which has to be stored, distributed and processed, not to mention that a capable instrument for performing various LHC-related simulations is needed as well. This task is carried out via the Worldwide LHC Computing Grid which connects over 170 computing centers located in 36 countries around the globe and is currently the world's largest distributed computing grid.

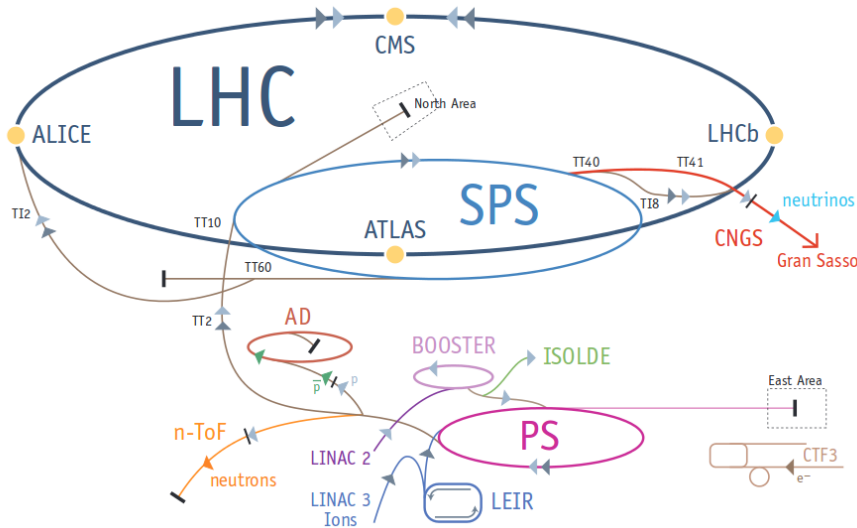


Figure 3.1: Schematic view of the CERN's accelerator system including the LHC. Taken from [20]

As mentioned above, the particles are meant to collide in one of the four interaction points where the detectors are placed. The ATLAS (A Toroidal LHC ApparatuS) is the biggest of these particle detectors. It is a general purpose detector (like the CMS) whose main original aim was to find the Higgs boson. That particle was eventually found in 2012 [2],[3] and the detector is now intended to be used to examine the Standard Model more precisely and to look for signs of a new physics beyond the SM, e.g. extra dimensions or new elementary particles.

Main parts of the detector can be seen in Figure 3.2. After the interaction occurs, produced particles firsts encounter the Inner Detector whose purpose is to track charged particles, i.e. it measures their direction, momentum and charge. This is realized by the magnetic field which causes charged particles to curve. The direction of the curve reveals information about particle charge and the magnitude of the curvature determines its momentum. The Inner Detector covers the entire region of the azimuthal angle ϕ and a region of pseudorapidity $|\eta| < 2.5$. It consists of three main components - Pixel Detector, Semiconductor Tracker and Transition Radiation Tracker.

The next layer of the ATLAS detector is composed of two calorimeters which measures the energy of charged and neutral particles as they interact with the material of the detector. A calorimeter consists of layers of an active medium, e.g. liquid argon, interspaced by layers of an absorbing high-density material such as lead. Therefore most of the particles coming from the collision deposit all of their energy inside the detector. Closer to the center of the detector a barrel electromagnetic calorimeter is placed which detects the energy of electrons and photons, and is surrounded by the forward EM calorimeters and the end-cap. Behind the EM calorimeters a hadronic Tile Calorimeter is located. Together with the hadronic forward calorimeter and its end-cap it measures the deposited energy of hadrons. Overall acceptance of the ATLAS calorimeters lies in the region of pseudorapidity $|\eta| < 4.9$.

Some of the particles mostly do not interact with matter and therefore do not stop in calorimeters and continue along its path out of the detector. One of these particles is muon. To capture them, a huge Muon Spectrometer consisting of 4000 individual muon chambers surrounds the calorimeters.

The detector is also equipped with two large superconducting magnet systems. The inner solenoid one produces magnetic field of approximately 2 T and surrounds the Inner Detector. Outside the calorimeters, eight large air-core superconducting barrel loops and two end-cap magnets produce the outer toroidal magnetic field which varies between 2 and 8 T. As mentioned above these magnets curve the trajectory of a charged particle, providing the information about its momentum.

The ATLAS detector is also complemented by a set of various forward detectors located up to hundred meters from the interaction point in the LHC tube. These detectors are: Cerenkov detector LUCID located at a distance of ≈ 17 m from the interaction point, Zero-Degree Calorimeter located at ≈ 140 m from interaction point and ALFA at ≈ 240 m from interaction point. Also the AFP detector is currently being installed [21].

Beacuse of the large amount of the data produced by the detector, an efficient sorting system had to be implemented. The ATLAS uses so called Trigger System to reduce the flow of data and select desired events for physics analyses. The selection is carried out in three stages. The Level-1 trigger reduces, by determination of so called Regions-of-Interest which contain promisingly looking objects, the amount of information from the calorimeters and muon spectrometer from 40 million bunch crossings per second to approximately 100 000. Only few thousand events per second are then allowed to continue through Level-2 to Level-3 trigger (called event filter) which perform a rather detailed analysis of the full event data leaving about 200 events per second which are passed on to a data storage system for offline analysis. Very detailed description of the ATLAS detector and its components can be found in [22].

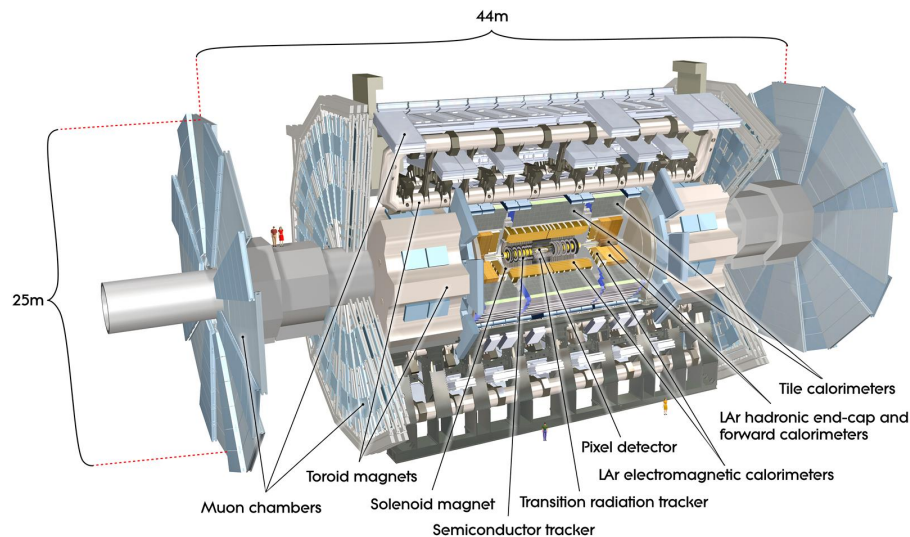


Figure 3.2: A computer generated picture of the ATLAS detector and its main parts. Taken from [23].

Chapter 4

Monte Carlo Generators and Jets

4.1 MC Generators

General-purpose Monte Carlo generators allow us to produce exclusive simulations of high-energy collisions. They are an important part of all experiments and also are widely used by theorists to create predictions for future experiments. Examples of such generators are various versions of PYTHIA [24] or HERWIG [25] and also many specialized generators are available. For the propagation of the particles through the matter of the detector, a specialized software package called GEANT4 [26] is used.

In general, MC generators are based on Monte Carlo methods which obtain numerical results from repeated random sampling. Therefore MC event generators used in high-energy particle physics try to randomly generate events with the same probability as they are produced in accelerators. The structure of a pp collision is shown in Figure 4.1. Generation of a particular event follows this evolution to provide the simulation of the whole process from the collision to the final-state particles which in real collisions are captured in a detector. If we are interested in hard QCD processes, the simulation starts in the center of collision and probability distribution of the scatter is calculated from perturbative theory. After that a parton shower phase follows. As the electrically charged particles radiate photons through Bremsstrahlung process and colour charged particles radiate gluons, which can also radiate a new gluon itself thanks to SU(3) properties, the phase space fills up with the products of parton shower. The evolution of the parton shower can be described by perturbative approach. As parton shower propagates, momentum scales lower down to a level where perturbation theory can not be used anymore. At this stage phenomenological hadronization models are used to describe the hadronization process as the particles confine themselves into colorless hadrons which are to be detected. However some of these hadrons may further decay. Also there is a possibility that besides the hard scatter, other multiparton interactions and rescatter of the beam remnants may occur, producing soft particles which contaminate the original hard process. These effects give rise to the so called underlying event which is the subject of research and improvements in our understanding of the collision process and its simulation. More information on the topic can be found in [27].

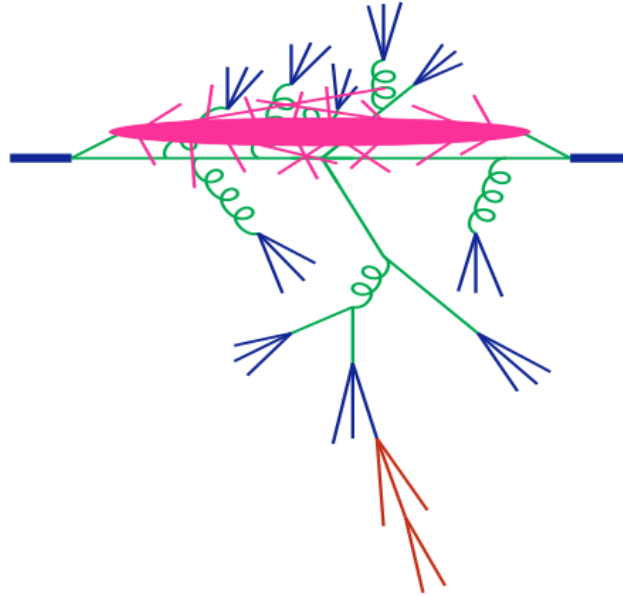


Figure 4.1: Diagram showing the evolution of a pp collision. Green colour denotes the parton shower, blue hadronization process, red decay of unstable particles and pink colour corresponds to underlying event. Diagram taken from [27]

4.1.1 Pythia 8

PYTHIA 8 is a MC event generator of high-energy collisions based on C++ programming language. It was created by rewriting previous Fortran based versions and including several improvements and new physics aspects. PYTHIA 8 contains complex set of physics models allowing the simulation of the above-described processes. Various libraries and models for parton showers, multiparton interactions, beam remnants behavior and particle decays are included. It can also be linked with external programs, e.g. ROOT. The program is able to work with pp , $p\bar{p}$, e^+e^- and $\mu^+\mu^-$ beams providing a hard scatter simulation of these incoming beams and also the evolution of the following processes such as parton shower and hadronization, which is based on Lund string model. From our point of view it is very important to point out that PYTHIA 8, as one of the few generators, is able to simulate the diffractive events which we would like to examine. More information is provided in [24].

4.2 Jets

Jets represent collimated sprays of particles produced in hard QCD processes from initial parton. We can distinguish three "levels" of jets based on the time of the evolution of the collision. A parton-level jet can be identified immediately after the collision. This is the level where one can use the perturbative QCD calculations. As the particles propagate themselves, they interact via strong force and create colorless composite particles, hadrons. At this level we use the term particle jet or true jet. This is also the level at which MC generators perform the predictions. Finally we can experimentally observe a detector level jet whose characteristics are based on calorimeter towers and/or on the tracks from tracking devices. They are clustered in pseudorapidity y and azimuthal angle ϕ region according to a chosen algorithm.

Given jet algorithm therefore provides a link between an initial parton and detected final-state particles, combining hadrons into jets according to a given radius R . Jets are defined by the choice of an appropriate algorithm and set of its input parameters. An ideal jet algorithm should have several convenient properties. First of all it has to satisfy theoretical requirements. The procedure must be collinear and infrared safe, meaning the invariance of the calculation to the radiation of collinear (nearly parallel) or soft (e.g. low energetic gluon) particle. This is related to the requirement on finite value of cross-section of the process at any order of the perturbative theory. An algorithm should also be well defined, independent of the experiment and effective, because we would like to obtain results in a reasonable time.

Jet algorithms can be divided into two categories. The cone algorithms are "top-down" approaches. As their name implies, they use the cone of a given radius R to incorporate particles in the surroundings of so called seeds, which are the prominent high energetic particles being suspected of belonging to particular jet. The disadvantage of cone algorithms is their possible collinear and infrared safety violence. The second type are sequential clustering algorithms which represent a "bottom-up" approach. In that they rely on recombination of two closest objects - a jet candidate and a hadron - in momentum up to a given distance R . The distance between objects is defined as

$$d_{ij} = \min(k_{T,i}^{2p}, k_{T,j}^{2p}) \frac{\Delta R_{ij}^2}{R^2} \quad (4.1)$$

where $k_{T,i}$ is the transverse momentum of particle i , R is the jet radius, p parametrizes the type of algorithm: $p = 1$ for k_t , $p = 0$ for Cambridge/Aachen and $p = -1$ for anti- k_t . ΔR_{ij} is defined as

$$\Delta R_{ij} = \sqrt{(y_i - y_j)^2 - (\phi_i - \phi_j)^2} \quad (4.2)$$

with y_i being the rapidity of object i and ϕ_i the azimuthal angle. Also a distance between object i and the beam (B) is defined as

$$d_{iB} = k_{T,i}^{2p}. \quad (4.3)$$

The clustering algorithm identifies smaller of the two distances, given by Eq. (4.1) and Eq. (4.3). If the smaller one is d_{ij} , objects i and j are recombined. If it is d_{iB} , object i is labeled as a jet and it is removed from the list of candidates. After that, distances are recalculated and process repeats until there are no objects left in the list. The advantage of sequential clustering algorithms is their collinear and infrared safety, although they can be slightly slower than cone algorithms. Three introduced sequential clustering algorithms and the SIScone cone algorithm are compared in Figure 4.2. Figure shows a simulated pp event at parton-level, with random soft particles (called "ghosts"), clustered with the four above mentioned algorithms and active catchment areas of resulting hard jets. Currently the most widely used jet algorithm is the anti- k_t clustering sequential algorithm implemented in FastJet package [28].

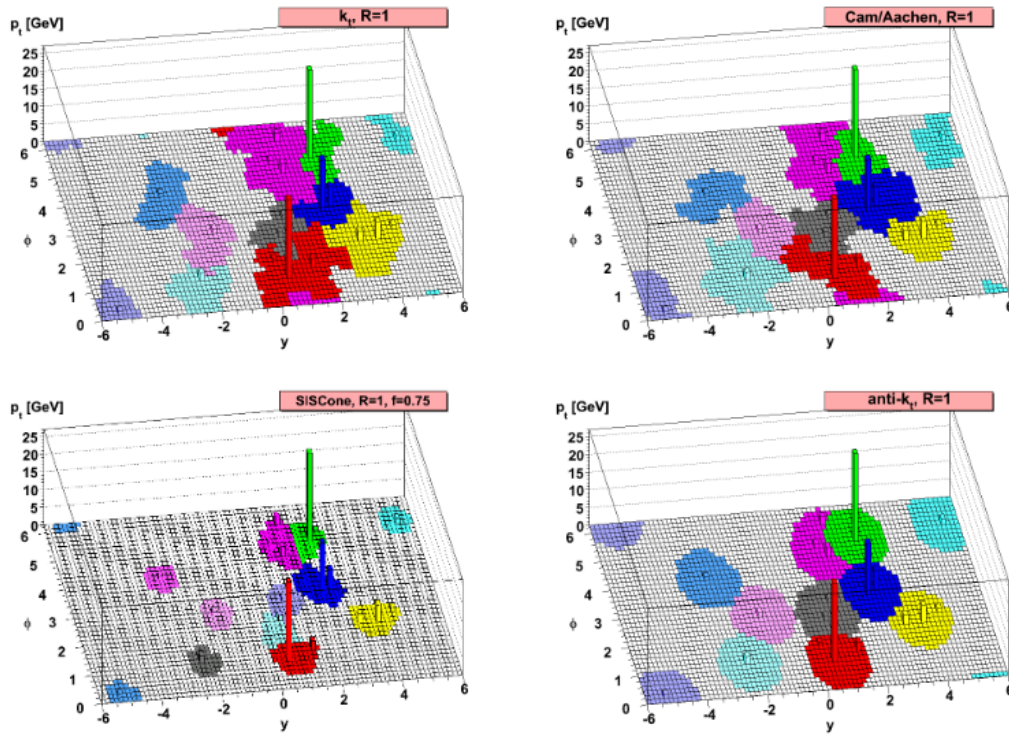


Figure 4.2: A simulated pp event at the LHC with jets reconstructed in rapidity y and azimuth ϕ phase space. Resulting hard jets clustered with k_t , Cambridge/Aachen, SISCone and anti- k_t algorithm for radius $R = 1$ are shown. Taken from [29]

Chapter 5

Results

The main object of this work is to study properties of the diffractive processes. We focus particularly on single diffraction (SD) and its characteristic properties. Also the comparison with double diffractive (DD) and non-diffractive (ND) processes is included.

First part of the chapter is devoted to the transverse energy E_T flow through the ATLAS detector and the examination of its sum and the transverse energy density $E_T^{density}$ in six regions of pseudorapidity in the interval $|\eta| < 4.8$. The goal of this task was to check whether Pythia 8 describes the ATLAS data correctly and thus may be used to study basic event characteristics at particle level and also to find out whether the properties of jet constituents are well described.

Acquired knowledge is then used to produce simulations of diffractive and also non-diffractive events and examination of its properties in two cases, the inclusive events, which are dominated by soft processes, and dijet events defined by an existence of at least two jets with transverse momentum $p_T > 20$ GeV. Moreover for the distribution of the most characteristic attribute of diffractive processes, called rapidity gap, not only shapes but also differential cross-sections are studied and compared to the published ATLAS data.

For these purposes, samples of pp collisions data at the center-of-mass energy $\sqrt{s} = 7$ TeV were generated using Monte Carlo generator Pythia 8.186 [24] and further processed using the data analysis system ROOT 6.02/08 [30] which is the C++ based object-oriented framework used for analysis in the field of particle physics. For dijet events, the anti- k_t clustering algorithm from the FastJet package [28] with the jet radius $R = 0.6$ was used.

5.1 Transverse energy flow in the ATLAS detector

Measurements of the sum of transverse energy of particles as a function of their pseudorapidity $|\eta|$ were carried out with the ATLAS detector and published in [31]. The analysis in the paper was performed using data taken during the first LHC runs in 2010 at the center-of-mass energy $\sqrt{s} = 7$ TeV. Minimum bias data samples for inclusive proton-proton interactions were used with integrated luminosity $7.1 \mu\text{b}^{-1}$, which is rather small due to low instantaneous luminosities during first LHC runs, providing insignificant contribution from multiple pp interactions. Measurements are performed in the region of pseudorapidity $|\eta| < 4.8$ making use of the entire acceptance $|\eta| < 4.9$ of the ATLAS calorimeters. In the first part of our analysis we try to reconstruct these measurements with the Pythia 8.186 MC generator using process option SoftQCD:All and compare its predictions with the data.

In total 10^6 events were generated. Following the prescription for selection of particles in the minimum bias dataset used in [31], we accept only events which contain at least two charged final state particles with the transverse momentum $p_T > 250$ MeV and $|\eta| < 2.5$. Sum of the transverse energy $\sum E_T$ is defined at the particle level as the sum of transverse energy E_T of all stable neutral particles with momentum $p > 200$ MeV and all stable charged particles with $p > 500$ MeV. These conditions on momentum p take into account fact, that particles with lower momentum deposit negligible amount of energy in calorimeters. The $\sum E_T$ distribution is compared in six regions of pseudorapidity: $0.0 < |\eta| < 0.8$, $0.8 < |\eta| < 1.6$, $1.6 < |\eta| < 2.4$, $2.4 < |\eta| < 3.2$, $3.2 < |\eta| < 4.0$ and $4.0 < |\eta| < 4.8$ and it can be defined as $\frac{1}{N_{event}} \frac{dN_{event}}{dE_T}$. As we can see the $\sum E_T$ distribution is normalized by number of events N_{event} . We also examined the mean $\sum E_T$ per unit area $\Delta\eta \cdot \Delta\phi$, which is defined as

$$E_T^{density} = \left\langle \frac{d^2 \sum E_T}{d\eta d\phi} \right\rangle \approx \frac{1}{N_{event}} \cdot \frac{1}{2\Delta\eta} \cdot \frac{1}{\Delta\phi} \cdot \sum_{x < |\eta| < y} (\sum E_T) \quad (5.1)$$

where $\Delta\eta = 0.8$ and $\Delta\phi = 2\pi$ rad.

In Figure 5.1 and Figure 5.2 the distributions of $\sum E_T$ and $E_T^{density}$ in six regions of $|\eta|$ are shown. In both figures we can see the predictions of Pythia 8.186 MC generator, including its statistical errors, compared to the ATLAS data analyzed in [31]. Both statistical and systematic errors are taken into account for the data. We observe a good agreement between the data and predictions of Pythia 8.186. In all bins the differences are within 20%. Taking into account the fact that we used the default version of Pythia 8.186 without any additional tuning, this result is viewed as satisfactory

We also observe that particles with high E_T are very rare to occur in forward directions and are concentrated mostly in the more central regions of the detector. Now let us take a closer look at Figure 5.2 where the distribution of $E_T^{density}$ is depicted, which is calculated using mean values of distributions in Figure 5.1 - see Eq. (5.1). The highest values of $E_T^{density}$ are appearing in the region of pseudorapidity $1.5 < |\eta| < 3.0$ which is rather surprising thing as we would expect it to be highest in the most central region, i.e. for $|\eta| < 1$. In the most forward region there is significant decrease of the $E_T^{density}$ as could be expected from previous discussion on $\sum E_T$. In general, we can state that predictions of Pythia 8.186 MC generator for transverse energy density are slightly overestimated for $|\eta| < 3$ and on the other hand are little bit underestimated for the highest values of pseudorapidities $|\eta| > 4$ when compared to the data, but again all of the observed differences are within 20%.

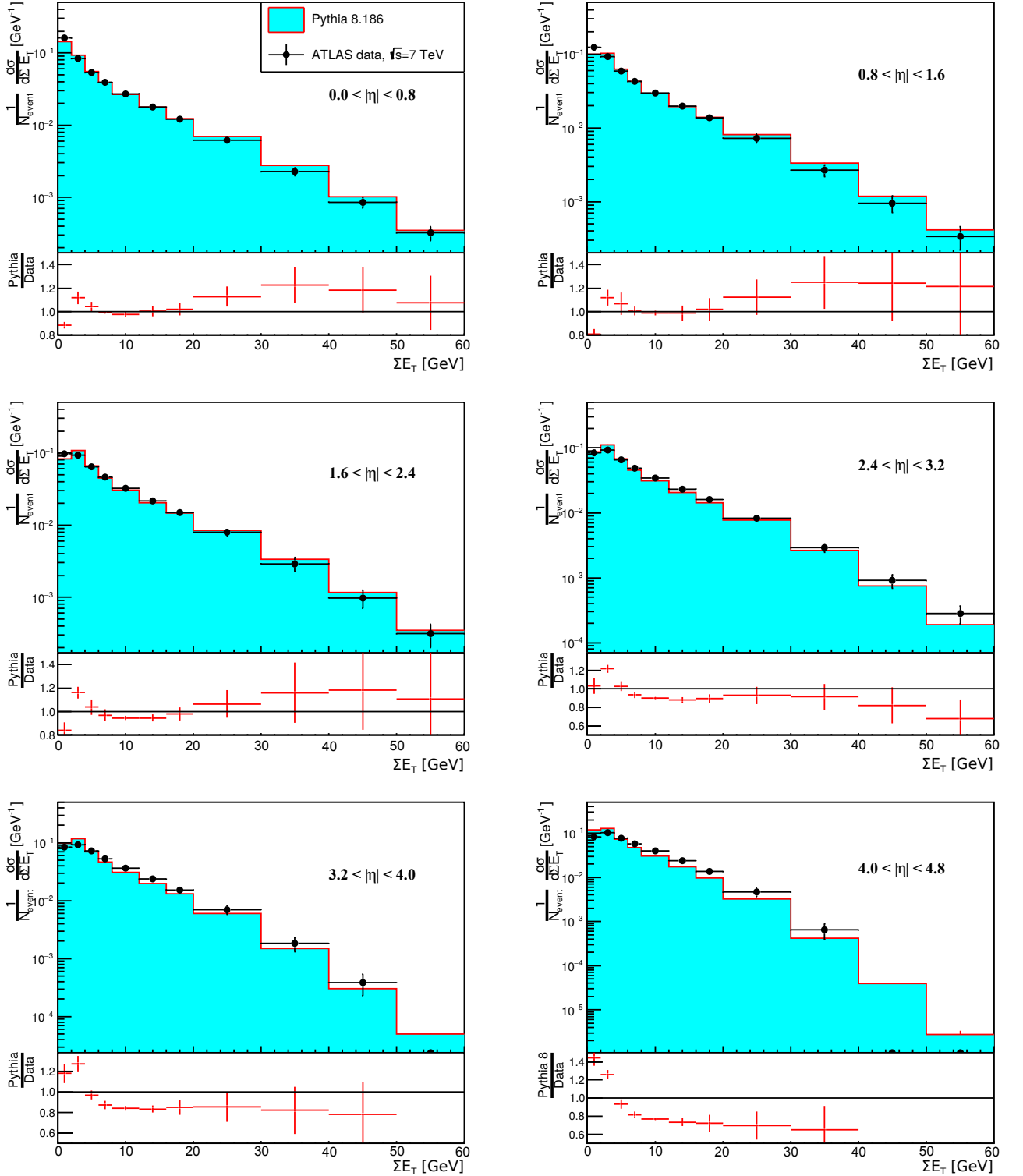


Figure 5.1: Transverse energy sum ΣE_T distributions of the data from [31] compared to Pythia 8.186 predictions for the minimum bias selection in six regions of pseudorapidity η : $0.0 < |\eta| < 0.8$, $0.8 < |\eta| < 1.6$, $1.6 < |\eta| < 2.4$, $2.4 < |\eta| < 3.2$, $3.2 < |\eta| < 4.0$ and $4.0 < |\eta| < 4.8$. Statistical and systematic errors are shown for the data and statistical errors only are displayed for the Pythia 8 model.

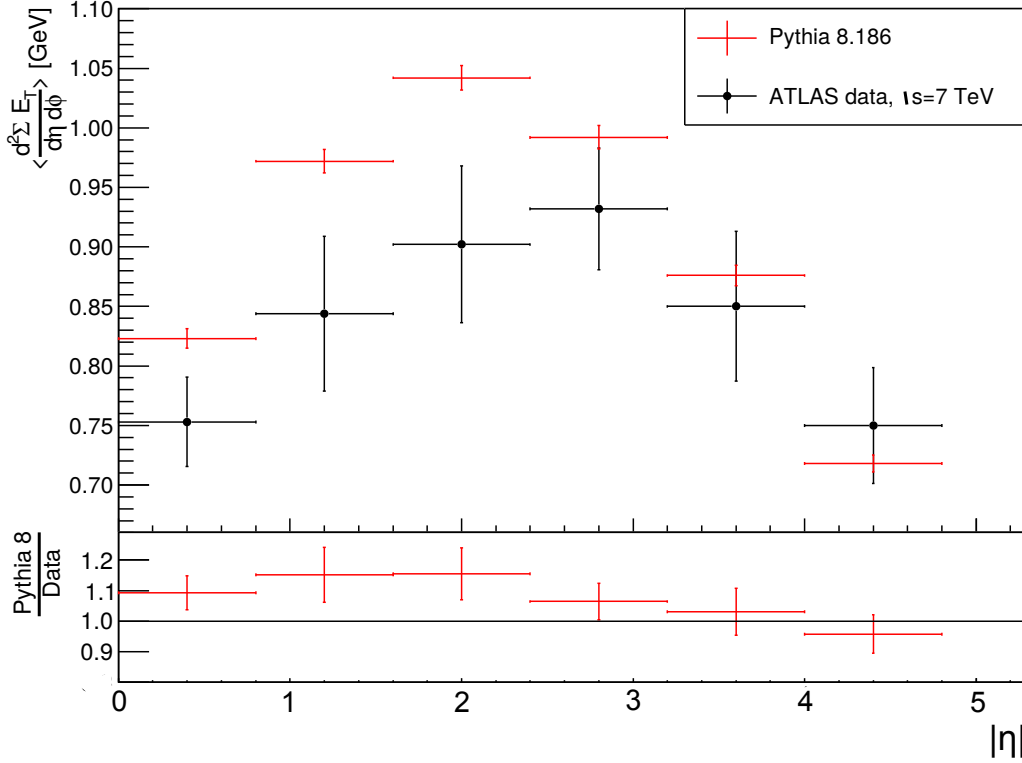


Figure 5.2: Transverse energy density $E_T^{density} = \left\langle \frac{d^2 \sum E_T}{d\eta d\phi} \right\rangle$ distribution of the data from [31] compared to Pythia 8.186 model for the minimum bias selection. Statistical and systematic errors are shown for the data and statisticals errors only are displayed for the Pythia 8 model.

5.2 Pomeron flux in inclusive and dijet single diffractive events

In this section we introduce distributions of ξ in various pomeron fluxes available in Pythia 8 settings. The term pomeron flux comes from the Regge theory and depends solely on ξ , which is the fractional momentum loss of the incident proton, and on the squared four-momentum transfer of the proton t . Further details can be seen in Chapter 2. For the MBR flux, which is used in further analyses, we will also investigate the t variable.

The environment of Pythia 8.186 offers five different pomeron flux models which affect the mass spectrum of diffractive system and the t spectrum of the exchange [32].¹ Their comparison can be seen in Figure 5.3 for inclusive single diffractive events and in Figure 5.4 for SD events where at least two jets with $p_T > 20$ GeV were required. The Schuler-Sjöstrand (option 1) and Bruni-Ingelman (option 2) fluxes are based on critical pomeron which is the strong-coupling solution of Reggeon Field Theory [33] and a conventional Pomeron description is the basis of Berger-Streng (option 3) and Donnachie-Landshoff (option 4) fluxes. The Minimum Bias Rockefeller (MBR, option 5) flux is based on simulations of (anti)proton-proton collisions and offers various optional parameters. The MBR flux provides the most satisfactory description of SD dijet events, based on results from CMS [34], and therefore it was chosen

¹Since the version 8.2, Pythia offers 7 different fluxes - H1 fit A and H1 fit B parameterizations of the pomeron flux were added to the five above listed fluxes.

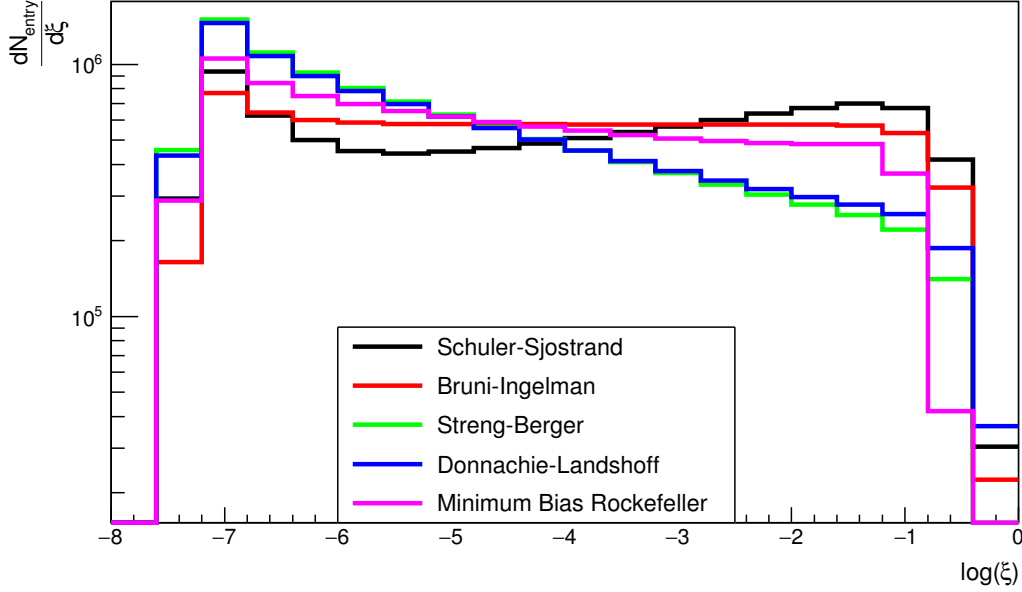


Figure 5.3: Distributions of ξ in inclusive SD events for different pomeron fluxes in samples generated using Pythia 8.186 at $\sqrt{s} = 7$ TeV.

to be used in our further examination of the properties of diffractive processes. Therefore also a t behavior for MBR flux is shown in Figure 5.5 for inclusive SD events and in Figure 5.6 for SD dijet events. Further information on fluxes and various diffraction parameters can be found in [32] or [35].

As we can see in Figure 5.3 all fluxes provide a steep rise in small values of ξ reaching its maximum at $\approx 10^{-7}$. For larger values of ξ all distributions are nearly flattened out, only Berger-Streng and Donnachie-Landshoff fluxes rather show a small decrease. All fluxes then drop at very high values of $\xi \approx 1$, especially Minimum Bias Rockefeller flux.

In Figure 5.4, when compared to the inclusive case in Figure 5.3, we see very low values of ξ being completely cut out, then a slow rise is observed up to the values around $\xi \approx 10^{-1} - 10^{-0.5}$ where a sudden drop occurs. It implies that cases with higher fractional momentum loss of the incident proton are preferred in SD dijet events, which is indeed expectable as the condition on jet's p_T requires particles with relatively high p_T in the central detector and hence large invariant masses of the system as $\xi \approx \frac{M_X^2}{s}$.

Let us now examine the squared four-momentum transfer of the proton t defined in the Eq. (2.18). As mentioned above, the data for t dependence were generated using MBR pomeron flux. For inclusive SD, the cases with $t \rightarrow 0$ are preferred, followed by a steep decrease towards strongly suppressed higher values, indicating that most of the SD events occurs at small t , giving very forward protons. On the other hand in dijet SD events values of $t \rightarrow 0$ are little bit suppressed, resulting in a small shift of the distribution's maximum towards higher values of t . Because we are still talking about single diffraction, a forward proton is obviously present causing high suppression of high t cases just like in inclusive SD events.

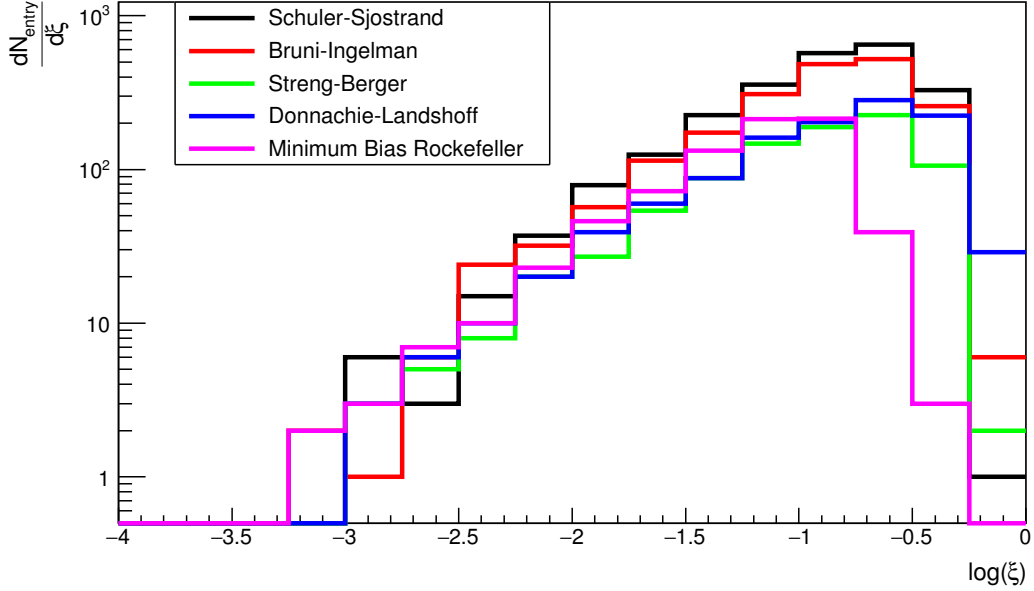


Figure 5.4: Distributions of ξ in dijet SD events for different pomeron fluxes in samples generated using Pythia 8.186 at $\sqrt{s} = 7$ TeV. Events are selected by requirement on at least two jets with $p_T > 20$ GeV.

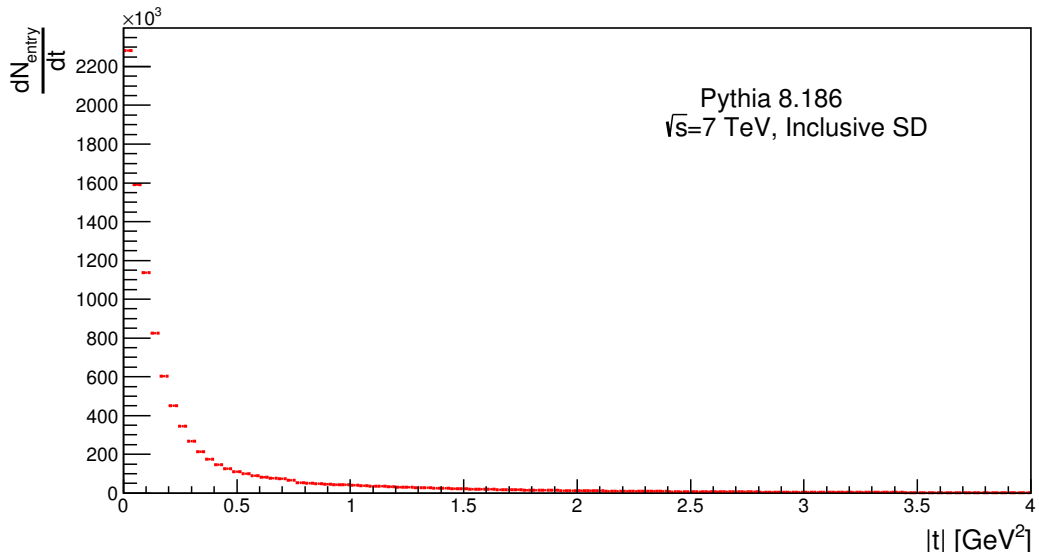


Figure 5.5: A t distribution for inclusive SD events in sample generated by Pythia 8.186 using MBR pomeron flux at centre-of-mass energy $\sqrt{s} = 7$ TeV.

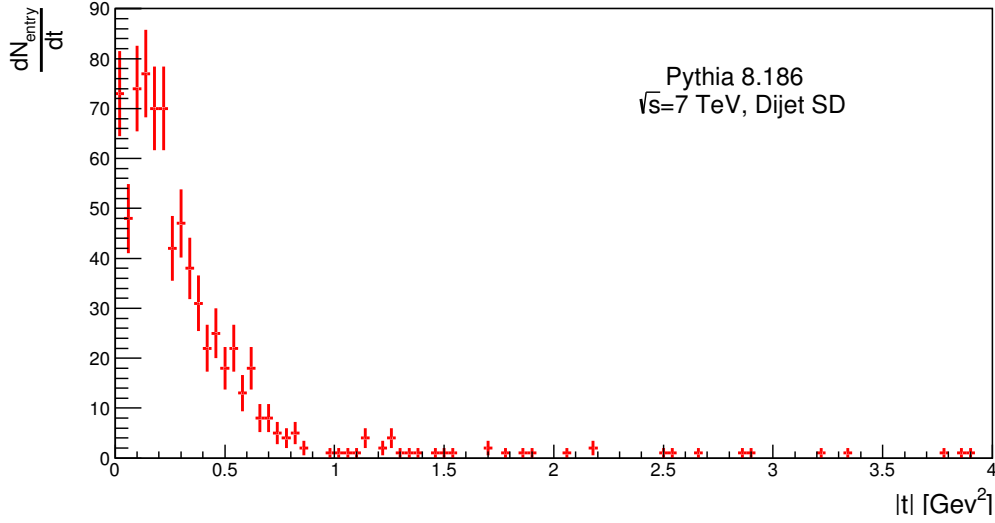


Figure 5.6: A t distribution for dijet SD events in sample generated by Pythia 8.186 using MBR pomeron flux at $\sqrt{s} = 7$ TeV. Events are selected by requirement on at least two jets with $p_T > 20$ GeV.

5.3 Characteristic particle properties of diffractive events

In this part we will focus on the description of characteristic particle properties of single diffractive events and their comparison with double diffractive and non-diffractive cases. For each case an amount of 10^7 pp collisions at the center-of-mass energy $\sqrt{s} = 7$ TeV was generated using the MC generator Pythia 8.816 with option SoftQCD:All and MBR pomeron flux. The goal is to examine the properties such as invariant mass of the system M_X or number of charged particles in the event n_{ch} applying the same cuts used at detector level. Accordingly only the particles with pseudorapidity $|\eta| < 4.9$ and transverse momentum $p_T > 200$ MeV were accepted. Particles with higher pseudorapidity could not be detected in the central detector's calorimeters and lower momentum particles do not produce the tracks with suitable efficiency of the detection. In case of dijet events the anti- k_t algorithm with $R = 0.6$ provided in FastJet package [28] was used for jet reconstruction. A condition on existence of at least two jets with $p_T > 20$ GeV was implemented.

Invariant mass M_X of the dissociation system is one of the common variables describing diffraction (see Chapter 2). One can calculate it as

$$M_X = \sqrt{\left(\sum E_i\right)^2 - \left(\sum \mathbf{p}_i\right)^2}, \quad (5.2)$$

where E_i is the energy of particle i and \mathbf{p}_i is its momentum. In our calculation we accept only particles with $|\eta| < 4.9$ so we can include only the particles which would be captured in the central detector. There is also other way to obtain the invariant mass of the system in diffractive event. Using the center-of-mass energy \sqrt{s} of the collision and the fractional momentum loss of the incident proton ξ , it can be defined as

$$M_X = \sqrt{s} \cdot \xi. \quad (5.3)$$

The number of charged particles n_{ch} is rather a global quantity but it is very widely used in particle physics and often compared with theory calculations, which is why it is listed in our set of examined variables.

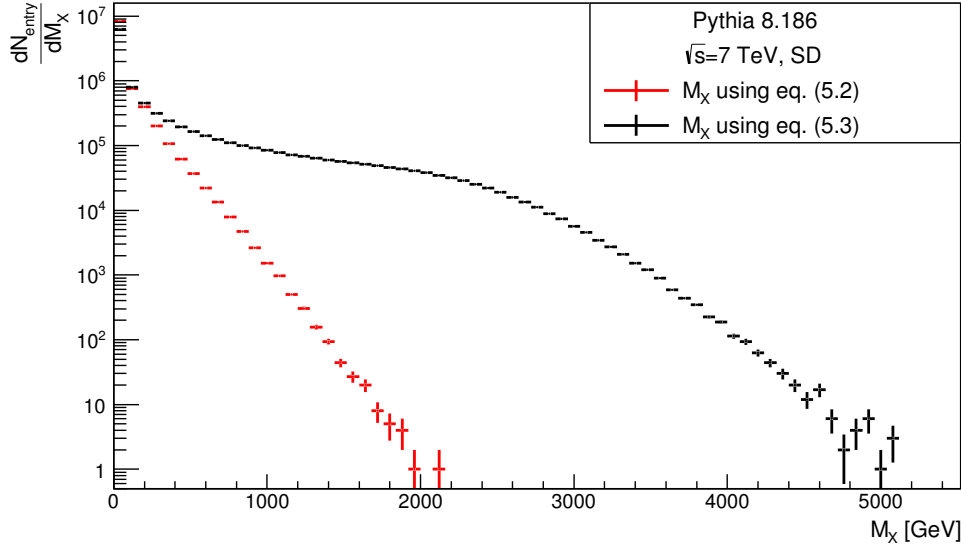


Figure 5.7: Invariant mass M_X distribution for inclusive SD events with MBR pomeron flux. Two methods of M_X calculation are presented in this graph. The red histogram corresponds to particles selected using cuts used to select objects on detector level, i.e. it depicts the calculation method using the Eq. (5.2), while the black histogram corresponds to usage of ξ obtained from the most forward proton, i.e. it corresponds to the Eq. (5.3).

5.3.1 Inclusive events

We compare the two above defined methods of calculating the invariant mass of the system for inclusive SD events in Figure 5.7 to indicate the big size of the uncovered forward region outside the central detector. For overview an invariant mass of the system in double diffractive and non-diffractive events is provided in Figure 5.8 where in order to provide a good interpretation, only Eq. (5.2) is used for the calculation.

As can be seen in Figure 5.7, the invariant mass shows a slowly decreasing tendency for high values of M_X , which indicates that processes with low M_X are present in inclusive events. This tendency is even more perspicuous in M_X calculated using the Eq. (5.2) because particles in forward directions $|\eta| > 4.9$ are not taken into account unlike in Eq. (5.3). In Figure 5.8 double diffractive invariant mass shows similar tendency as the single diffractive M_X . On the other hand ND invariant mass comes up to considerably higher values than diffractive ones.

Let us now take a closer look on the number of charged particles n_{ch} shown in Figure 5.9. The n_{ch} clearly reaches its maximum for very low values of n_{ch} in diffractive events, however in double diffractive events the maximum is slightly shifted toward higher values and the tail of the distribution ends in lower values of n_{ch} in contrast to single diffraction, difference is ≈ 20 . Whereas for ND the maximum is even more shifted reaching values ≈ 20 of n_{ch} with the tail continuing far behind the highest values of n_{ch} seen in diffractive cases. This is usually explained by the presence of the rapidity gap in diffractive process, which is a region devoid of particles or with extremely reduced hadronic activity.

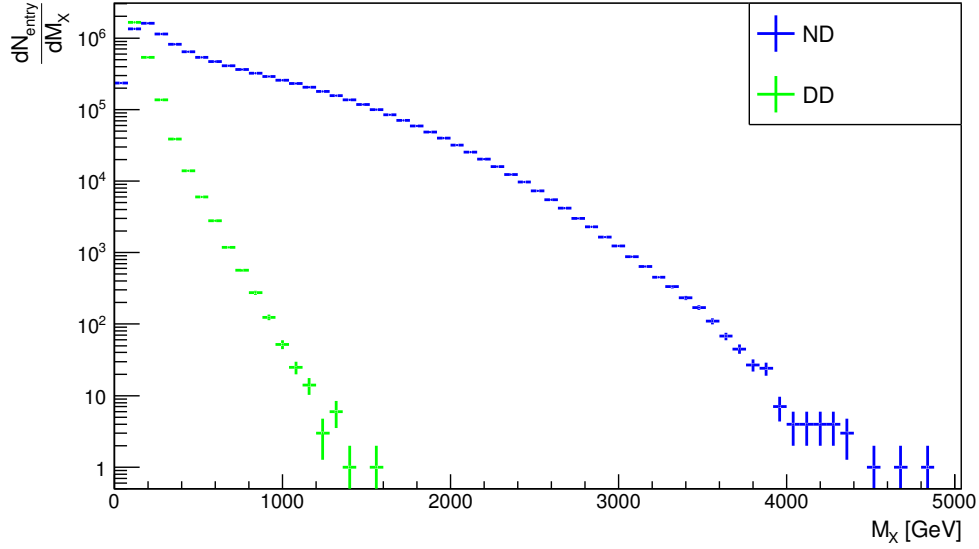


Figure 5.8: Invariant mass M_X distributions for inclusive DD and ND events in samples generated by Pythia 8.186 at $\sqrt{s} = 7$ TeV, both taking into account particles selected according to cuts used to select detector objects.

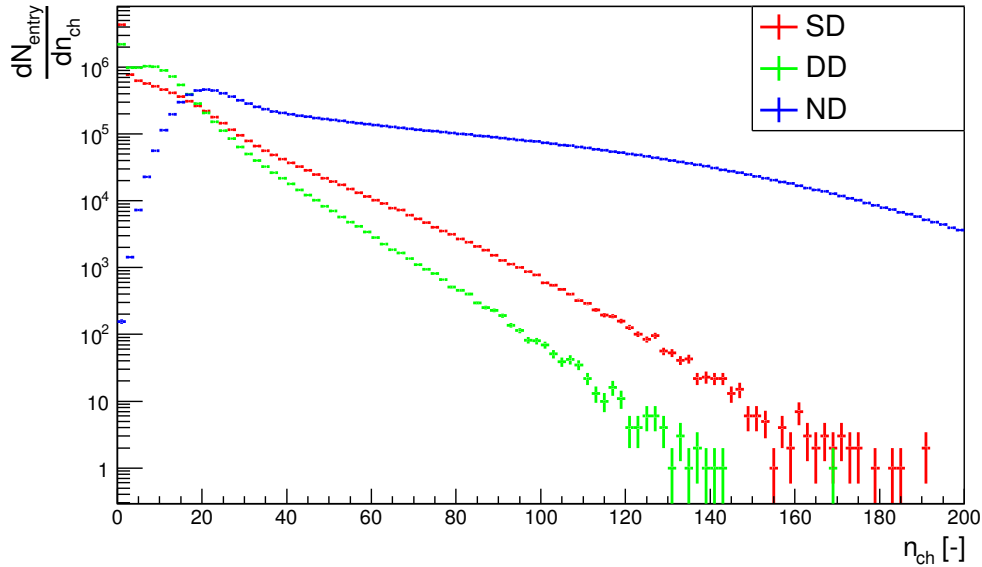


Figure 5.9: Number of charged particles n_{ch} distributions for inclusive single diffractive (red histogram), double diffractive (green histogram) and non-diffractive (blue histogram) events, samples being generated by Pythia 8.186 at $\sqrt{s} = 7$ TeV using MBR flux for diffractive events. The cut used to select objects at the detector level is applied.

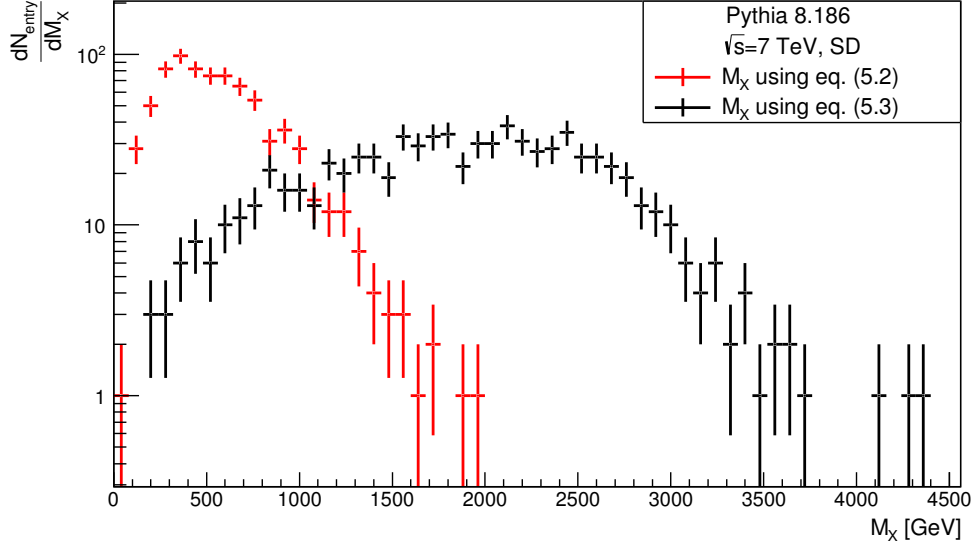


Figure 5.10: Invariant mass M_X distribution for dijet SD events, with MBR pomeron flux, where $p_{T_{jet}} > 20$ GeV. Two methods of M_X calculation are presented in this graph. The red histogram corresponds to particles selected using cuts used to select objects on detector level, i.e. it depicts the calculation method using the Eq. (5.2), while the black histogram corresponds to the usage of ξ obtained from the most forward proton, i.e. it corresponds to the Eq. (5.3).

5.3.2 Dijet events

Similar graphs as in Chapter 5.3.1 are presented also in this section, but for events where at least two jets with $p_T > 20$ GeV were required. This cut has a significant influence on invariant mass M_X and number of charged particles n_{ch} distributions. In Figure 5.10 we can see two already presented approaches for M_X calculation. Same assumptions concerning the difference between the calculation of M_X using the Eq. (5.2) or Eq. (5.3) can be made. However there is very significant change in the position of maximum. As can be seen, it is shifted towards higher values of M_X in both cases, thus events with very low M_X are deeply suppressed when compared to inclusive SD. The same tendency of suppression of the low M_X cases is present in double diffractive and non-diffractive processes as shown in Figure 5.11.

This suppression of lower values due to cut for jets is also noticeable in n_{ch} distribution in Figure 5.12. The relative difference in behavior of the distribution in the highest values of n_{ch} between SD and DD dijet events is quite similar to inclusive ones. As well in ND events the distribution goes far beyond the highest values of n_{ch} seen in diffractive cases, even more rapidly than in inclusive events. It is therefore obvious that a condition on existence of jets strongly affects the distributions of characteristic variables of diffraction by suppressing the lowest values, which is understandable because the presence of the jets requires either more particles in an event or particles with high p_T or, obviously, both of them.

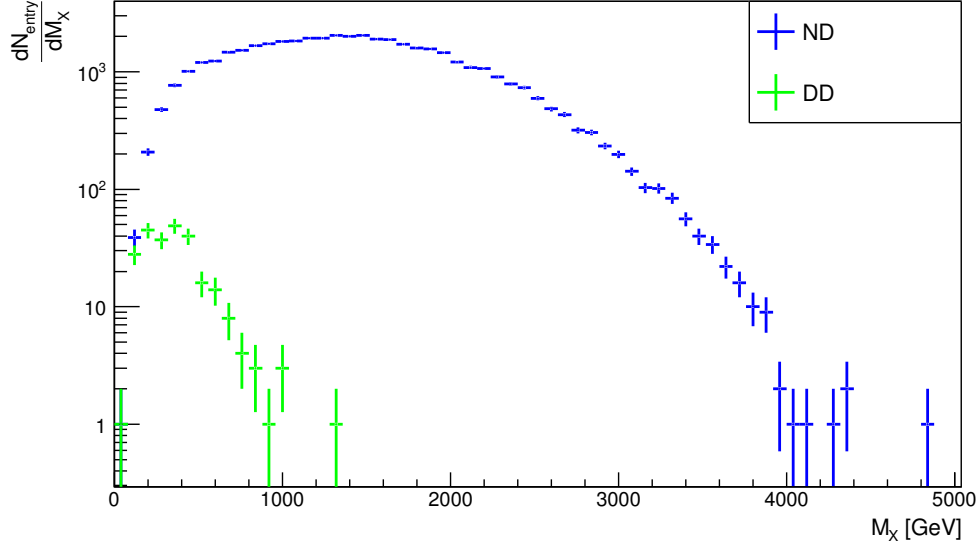


Figure 5.11: Invariant mass M_X distribution for dijet DD and ND events, where $p_{T_{jet}} > 20$ GeV. Samples were generated using Pythia 8.186 at center-of-mass energy $\sqrt{s} = 7$ TeV, both taking into account particles selected according to cuts used to select detector objects.

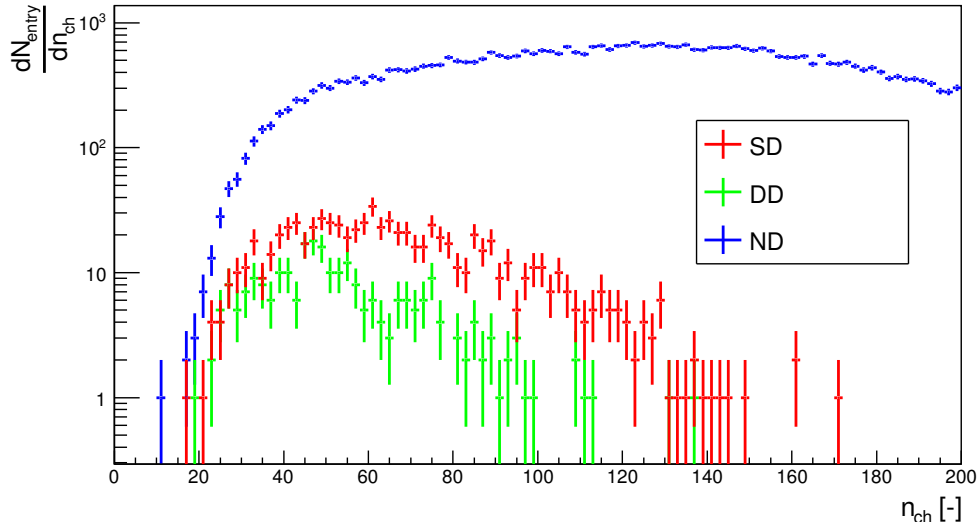


Figure 5.12: Number of charged particles n_{ch} distributions for dijet single diffractive (red histogram), double diffractive (green histogram) and non-diffractive (blue histogram) events, samples being generated by Pythia 8.186 at $\sqrt{s} = 7$ TeV using MBR flux for diffractive events. Events are selected by requirement on at least two jets with $p_T > 20$ GeV. and the cut used to select objects at the detector level is applied.

5.4 Rapidity gaps - inclusive and dijet and comparison with the data

Large rapidity gaps (LRG) are the regions of rapidity (or pseudorapidity) devoid of any hadronic activity. They are formed due to color singlet exchange in the t-channel associated with the pomeron exchange and therefore are one of the key features of diffractive processes. We usually use the pseudorapidity variable to define LRG. Size of a gap is obtained as a distance of the first occurring particle from the edge of our detector. Two gaps are found through this process, one identified from the edge located in positive values of z and one identified from the edge in negative values of z axis (i.e. the beams directions). The desired gap is then the bigger one of these two.

Measurements of the differential cross sections in forward rapidity gap size in pp collisions at $\sqrt{s} = 7$ TeV were performed with the ATLAS detector for inclusive events and published in 2012 [17], and for dijet events in 2015 [12]. In this section, we will try to reconstruct these measurements using Pythia 8.186 MC generator. For these purposes a samples of $5 \cdot 10^7$ events for SD and DD and 10^7 for ND processes were generated at the center-of-mass energy $\sqrt{s} = 7$ TeV. The MBR Pomeron flux was applied, as in previous examinations. In accordance with papers [12] and [17], the edge of the detector is located at $|\eta| = 4.9$, therefore expected gap sizes can be $\Delta\eta < 9.8$ and only particles with $p_T > 200$ MeV were accepted to the calculation process. Lower transverse momentum particles are not taken into account during the evaluation of the data because of the tracking acceptance.

In Figure 5.13 we can see the differential cross-section as a function of the gap size $\Delta\eta$ for inclusive SD, DD and ND events and their sum compared to the data from [17]. It is clearly obvious that in low $\Delta\eta$ values non-diffractive processes form the main contribution to the inelastic cross-section and single diffractive and double diffractive contributions are rather negligible. However with increasing $\Delta\eta$ the ND contribution falls exponentially and for $\Delta\eta \approx 3$ it is insignificant when compared to SD and DD. At high values of $\Delta\eta$ we observe a forming plateau caused by diffractive effects, SD and DD contributions are almost equal in these regions, and for values $\Delta\eta \approx 6$ and higher a slow rise of the differential cross-section occurs which is caused mainly by SD events. This rise is believed to be a consequence of the dynamics of SD and DD processes [17]. As can be seen from attached ratio plot in Figure 5.13, Pythia 8 describes the data reasonably in the region of $\Delta\eta < 3$ but at higher values of the gap size they do not describe the plateau and consecutive rise in the differential cross-section very well. This behavior is in agreement with observations made in [17] where Pythia 8 was also used for the simulations, but with a different tune called Pythia 8 4C and a Schuler-Sjöstrand pomeron flux. The double diffractive contribution to the inelastic cross-section seems to be very similar to the one in the [17]. However the single diffractive contribution is much smaller which is caused by the choice of pomeron flux. It is clearly obvious from Figure 5.3 that MBR flux causes bigger suppression of high values of ξ than Schuler-Sjöstrand flux. As these high values of fractional momentum loss of the proton cause events with small rapidity gaps, the contribution of the low $\Delta\eta$ cases is hence suppressed because of the MBR flux choice.

The differential cross-section as a function of the gap size with cut for at least two jets with $p_T > 20$ GeV is depicted in Figure 5.14. The anti- k_t clustering algorithm with radius $R = 0.6$ was used for the jet reconstruction. It is important to note that in the analysis presented in [12] a rather different cuts for the selection of particles were used compared to the analysis [17]. Here a gap is defined as a region of pseudorapidity absent of neutral particles with $p > 200$ MeV and charged particles with $p > 500$ MeV or $p_T > 200$ MeV. Similarly as in analysis [12], we normalized the ND contribution to match the data in the first gap bin. The normalization factor is 0.75 which is slightly different, but very close, with respect to the factor 0.71 used in [12]. The difference can be explained by the fact that the factor 0.71 comes from the detector-level comparison, however we are working at the particle level. As in the previous inclusive case the main contribution to the differential inelastic cross-section is produced by ND events in low values of $\Delta\eta$ where they fit the data reasonably, and with increasing $\Delta\eta$ ND is gradually

balanced by SD and DD contributions. The differential cross-section also falls exponentially for ND events. ND contribution seems to fit the data reasonably within first four bins and is also in accordance with the Pythia 8 model presented in [12], except the region $\Delta\eta$ where the disagreement is caused by the low statistics in our model. For SD and DD events and the sum we do not observe the plateau and the small rise of the cross-section as in the inclusive case depicted in Figure 5.13. Exponential tendency of the differential cross-section in Figure 5.14 is, together with the non-existing plateau, a consequence of reduced phase space available for the gap occurrence, caused by the requirement of at least two jets with $p_T > 20$ GeV. For a better consistency with simulations in analysis [12], SD and DD differential cross-sections as functions of the gap size are also provided using Donnachie-Landshoff flux choice. As can be seen from Figure 5.4, a suppression of high ξ cases is again present in the MBR flux, therefore a contribution of SD events is rather smaller in the region of low $\Delta\eta$ than the contribution of single diffractive events with D-L flux choice. Despite the same D-L flux used in our analysis and analysis [12], differences are seen for SD predictions. They may be caused by slightly different version of Pythia 8 and possible additional tunes used. Again no additional tunes were implemented in our case. Very interesting phenomenon may be observed for DD events. Contrary to SD events, for double diffraction Donnachie-Landshoff flux choice results up to 10 times lower values of differential cross-section than MBR flux. Sadly this phenomenon could not be compared to the results from [12] as DD case is not depicted separately there. The sum of SD, DD and ND contribution seems to be in accordance with the data and the simulations presented in [12] in the region of $\Delta\eta < 4$. For higher values of $\Delta\eta$ the model do not fit the data so accurately. But statistical uncertainties are not negligible in this region.

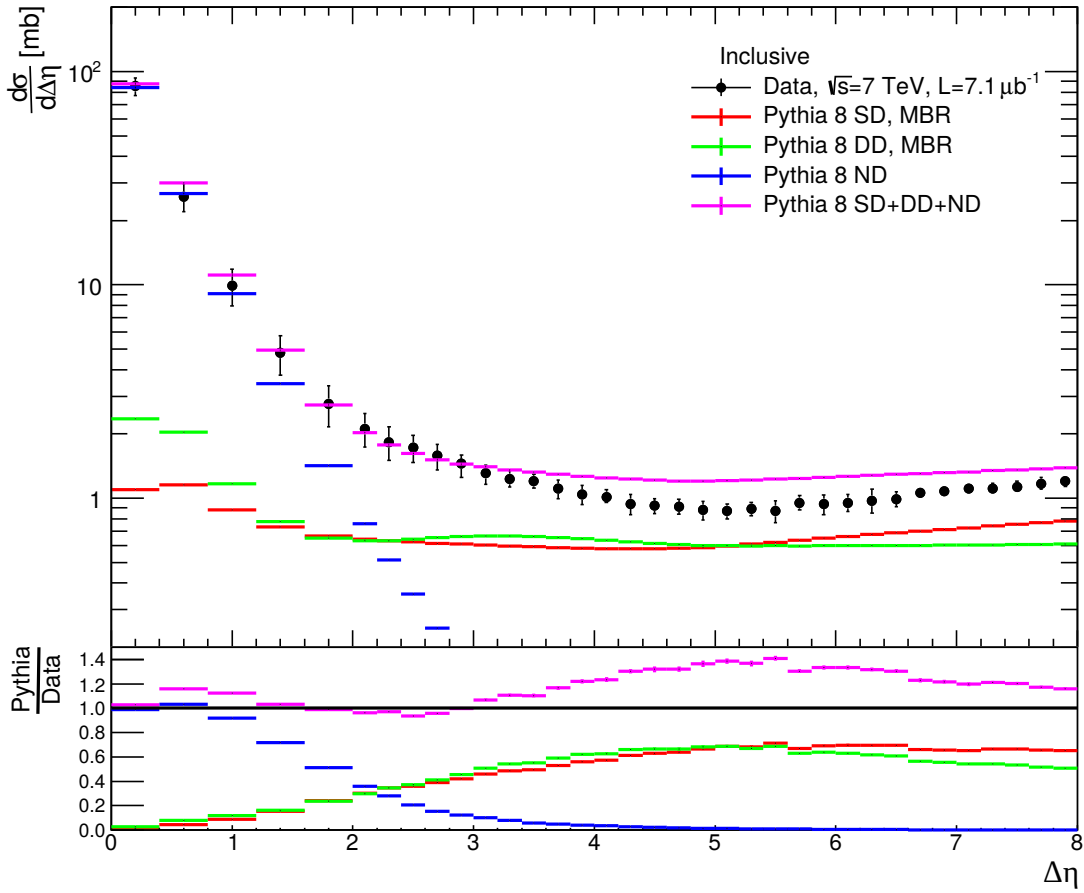


Figure 5.13: Inelastic differential cross-section in forward RG size $\Delta\eta$ for particles with $p_T > 200$ MeV and $|\eta| < 4.9$. The color lines shows predictions of Pythia 8.816 with Minimum Bias Rockefeller flux choice for inclusive SD, DD and ND events and their sum at $\sqrt{s} = 7$ TeV compared to the data from [17] depicted by the black dots.

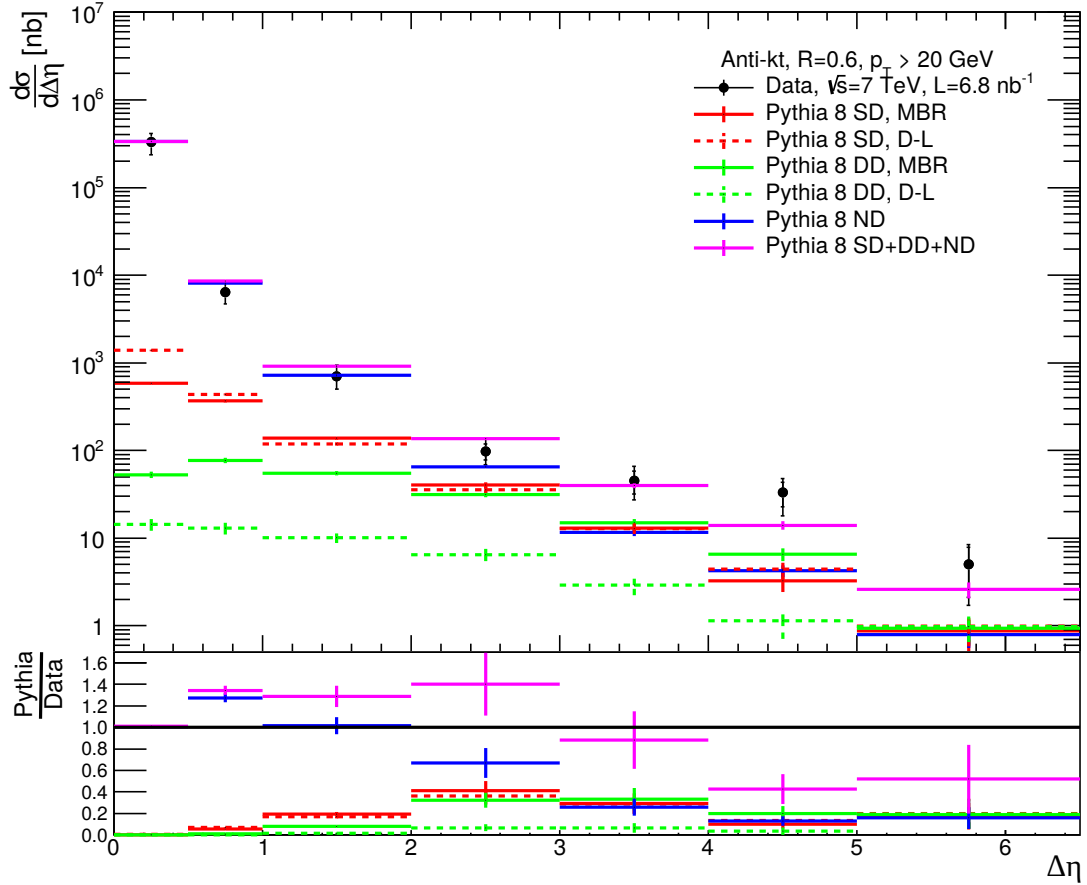


Figure 5.14: Inelastic differential cross-section in forward RG size $\Delta\eta$ for particles with $p_T > 200$ MeV, $|\eta| < 4.9$ and cut for two jets with $p_{T_{jet}} > 20$ GeV. The color lines shows predictions of Pythia 8.816 for dijet SD, DD and ND events and their sum at $\sqrt{s} = 7$ TeV compared to the data from [12] depicted by the black dots. Full lines represent the Minimum Bias Rockefeller pomeron flux, dashed lines represent Donnachie-Landshoff flux.

Conclusion

This thesis was devoted to the study of properties of diffraction processes. Therefore a summary on the theoretical description of the diffraction was provided, including the Regge theory which is important for the development of phenomenological models. Also the Standard Model and quantum chromodynamics were briefly introduced as tools for hard diffraction description. As we tried to compare inclusive events to dijet events, a short description of the jet properties and algorithms was also provided.

For the analysis a MC generator Pythia 8.186 was used. Acquired simulations were processed using data analysis framework ROOT 6.02/08 and the anti- k_t jet clustering algorithm provided in FastJet package was used for the jet reconstruction.

To check whether Pythia 8.186 with the original settings and no additional tunes can be used for studies of event and jet characteristics, a comparison with the ATLAS data measured at the center-of-mass energy $\sqrt{s} = 7$ TeV was carried out for the sum of the transverse energy of the particles $\sum E_T$ and for the transverse energy density $E_T^{density} \equiv \langle \frac{d^2 \sum E_T}{d\eta d\phi} \rangle$. Results of the task indicate that Pythia 8 without any additional tunes describes the data reasonably, as the observed differences are within 20 %.

Main topic of the work was a study of the properties in inclusive and dijet diffractive events. Dijet events were selected using the cut on existence of at least two jets with minimal transverse momentum $p_T > 20$ GeV and jet radius $R = 0.6$. First of all a comparison of the distribution of the fractional momentum loss of the incident proton ξ was provided for five available pomeron flux choices. For the rest of the analysis the Minimum Bias Rockefeller flux was chosen based on the CMS Collaboration results which consider this flux the best choice for the description of single diffractive dijet events. For an overview a square of the transferred four-momentum t distribution was compared for inclusive and dijet events using the MBR flux choice. Next a description of the invariant mass M_X of the single diffractive system was provided for two different approaches - one based on the ξ variable, see Eq. (5.3), and the other on the calculation using particle's momentum and energy, see Eq. (5.2). With an ideal detector coverage of the whole pseudorapidity region these two approaches should be equal. However as we used the cut on particle pseudorapidity $|\eta| < 4.9$ and transverse momentum $p_T > 200$ MeV in calculation using Eq. (5.2), providing a similar cut on particles as the one which is implemented on the objects registered in central detector, these two approaches give very different results. It indicates that a considerable amount of particles is being undetected as they are occurring in the region not covered by the central detector. For the detection of these particles, specialized forward detectors are needed. SD invariant mass was also compared to the DD and ND invariant masses, again for inclusive and dijet events and this comparison was also executed for the number of charged particles.

The very important feature of the diffractive events are large rapidity gaps which provide an effective tool for the detection of diffraction. Therefore there are great efforts to study this phenomenon. In this thesis we focused on the differential cross-section as a function of rapidity gap size. A discussion of Pythia 8 predictions for SD, DD and ND contribution to the inelastic cross-section and its comparison

to the published ATLAS data was performed. For inclusive events we acquired reasonably accurate results which were found to be in accordance with the data for low $\Delta\eta$ values where ND component gave the main contribution to the inelastic cross-section. However at values of $\Delta\eta \approx 3$ and higher an overestimation of the Pythia 8 prediction is clearly obvious and the plateau with subsequent rise of the differential cross-section was not observed. But this behavior is still in agreement with the Pythia 8 simulations performed in [17].

In dijet events we observe an exponential decrease of the total inelastic cross-section with increasing gap size which is governed by the dominant contribution of ND over almost all region of gap size. The plateau observed in inclusive events is not seen here as a consequence of the requirement on the presence of jets. Our simulations based on D-L flux are in a fair agreement with the data and more or less with simulations used in [12], especially in the region of lower values of $\Delta\eta$. Therefore we conclude that Pythia 8.186 without any additional tunes and parameter settings provides a good description of the ATLAS data which is also a conclusion achieved in the analysis [12]. This means that no soft survival probability S^2 is needed (i.e. $S^2 = 1.0$) for this particular model and pomeron flux. In the next steps, we are going to compare these ATLAS data with a more recent Pythia model 8.2 with dynamically generated value of S^2 [35].

Bibliography

- [1] M. C. Gonzales-Garcia and M. Maltoni, *Phenomenology with Massive Neutrinos*, Phys. Rept. 460 (2008) 1-129.
- [2] ATLAS Collaboration, *Observation of a new particle in the search for the Standard Model Higgs boson with the ATLAS detector at the LHC*, Phys. Lett. B716 (2012) 1-29.
- [3] CMS Collaboration, *Observation of a new boson at a mass of 125 GeV with the CMS experiment at the LHC*, Phys. Lett. B716 (2012) 30-61.
- [4] Standard Model of Particle Physics, University of Zurich webpage, 2015.
<http://www.physik.uzh.ch/groups/serra/images/SM1.png>
- [5] J. Chýla, *Quarks, partons and Quantum Chromodynamics*, University textbook, Prague, 2009.
<http://www-hep2.fzu.cz/Theory/notes/text.pdf>
- [6] D. H. Perkins, *Introduction to High Energy Physics, 4th edition*, Cambridge University Press, 2000, ISBN 0-521-62196-8.
- [7] A. Bettini, *Introduction to Elementary Particle Physics*, Cambridge University Press, 2000, ISBN 978-0-521-88021-3.
- [8] V. Petráček, *Subatomová fyzika I.*, University textbook for the course "Subatomic physics I", FNSPE CTU, Prague, 2009.
<http://physics.fjfi.cvut.cz/files/predmety/02SF/common/subatomovka-book-obr-zc12.2.10.pdf>
- [9] P. Růžička, *Diffraction in the ATLAS Experiment*, Doctoral thesis, 2012.
<http://www-hep2.fzu.cz/~vrba/RuzickaPavel-PhDThesis.pdf>
- [10] S. Donnachie, G. Dosch, P. Landshoff and O. Nachtmann, *Pomeron Physics and QCD*, Cambridge University Press, 2002, ISBN 0-521-78039-X.
- [11] O. Kepka, *QCD and Diffraction in the ATLAS Experiment at the LHC*, Doctoral thesis, 2009.
<http://okepka.web.cern.ch/okepka/files/phd.pdf>
- [12] ATLAS Collaboration, *Dijet production in $\sqrt{s} = 7$ TeV pp collisions with large rapidity gaps at the ATLAS experiment*, Phys.Lett. B754 (2016) 214-234.
- [13] UA8 Collaboration (R. Bonino et al.), *Evidence for Transverse Jets in High Mass Diffraction*, Phys. Lett. B211 (1988) 239.

- [14] H1 Collaboration (A. Aktas et al.), *Measurement and QCD analysis of the diffractive deep-inelastic scattering cross-section at HERA*, Eur.Phys.J. C48 (2006) 715-748.
- [15] M. Arneodo and M. Diehl, *Diffraction for non-believers*, 2005.
arXiv:hep-ph/0511047
- [16] V. Kûs, *Study of diffractive processes at the ATLAS Experiment*, Doctoral thesis, 2015.
<http://inspirehep.net/record/1381385/>
- [17] ATLAS Collaboration, *Rapidity gap cross sections measured with the ATLAS detector in pp collision at $\sqrt{s} = 7$ TeV*, Eur. Phys. J. C72 (2012) 1926.
- [18] T. Affolder et al. (CDF Collaboration), *Diffractive Dijets with a Leading Antiproton in $\bar{p}p$ Collisions at $\sqrt{s} = 1800$ GeV*, Phys. Rev. Lett. 84 (2000) 5043.
- [19] R. Staszewski, *Study of Diffraction with the ATLAS detector at the LHC*, Doctoral thesis, 2013.
<tel-00772329>
- [20] C. Lefevre, *LHC: The Guide (English version)*, 2009.
<http://cds.cern.ch/record/1165534/files/CERN-Brochure-2009-003-Eng.pdf>
- [21] ATLAS Collaboration, *Technical Design Report for the ATLAS Forward Proton Detector*, 2015.
ATLAS-TDR-024-2015
- [22] ATLAS Collaboration, *The ATLAS Experiment at the CERN Large Hadron Collider*, J. Instrum. 3 (2008) S08003.
- [23] J. Pequeno, Computer generated image of the whole ATLAS detector, 2008.
<http://cds.cern.ch/record/1095924>
- [24] T. Sjöstrand, S. Mrenna and P. Skands, *A Brief Introduction to PYTHIA 8.1*, JHEP05 (2006) 026,
Comput. Phys. Comm. 178 (2008) 852.
- [25] J. Bellm et al., *Herwig 7.0/Herwig++ 3.0 Release Note*, Eur. Phys. J. C (2016) 76: 196.
- [26] *Geant4 — a simulation toolkit*, Nuclear Instruments and Methods in Physics Research A506 (2003) 250-303.
- [27] M. H. Seymour and M. Marx, *Monte Carlo Event Generators*, Lectures from 69th Scottish Universities Summer School in Physics (SUSSP 69), 2012.
arXiv:1304.6677 [hep-ph]
- [28] M. Cacciari, G. P. Salam and G. Soyez, *FastJet user manual*, Eur. Phys. J. C72 (2012) 1896.
- [29] M. Cacciari, G. P. Salam and G. Soyez, *The anti- k_t jet clustering algorithm*, JHEP04 (2008) 063.
- [30] Documentation of the ROOT data analysis framework.
<https://root.cern.ch/documentation>
- [31] ATLAS Collaboration, *Measurements of the pseudorapidity dependence of the total transverse energy in proton-proton collisions at $\sqrt{s} = 7$ TeV with ATLAS*, J. High Energ. Phys. (2012) 2012:33.

- [32] Pythia 8.1 online manual - Diffraction.
<http://home.thep.lu.se/~torbjorn/pythia81html/Diffraction.html>
- [33] A. R. White, *The Pomeron in QCD*, published in:
P. A. Carruthers, *Hadronic Multiparticle Production*, World Scientific Publishing Co. Pte. Ltd., 1988,
ISBN 9971-50-558-4.
- [34] V. Khachatryan et al. (CMS Collaboration), *Measurement of diffractive dissociation cross sections in pp collisions at $\sqrt{s} = 7$ TeV*, Phys. Rev. D 92 (2015) 012003.
- [35] C. O. Rasmussen, T. Sjöstrand, *Hard Diffraction with Dynamic Gap Survival*, J. High Energ. Phys. (2016) 142.